Title page

Visualizing APP trafficking and processing reveals its association with neuronal membrane cholesterol

Authors

Claire E. DelBove[1], Claire E. Strothman[2], Hui Huang[3], Charles R. Sanders[3, 4], Qi Zhang[1]*

Affiliations

[1]Department of Pharmacology, Vanderbilt University

[2]Department of Cell and Developmental Biology, Vanderbilt University

[3]Department of Biochemistry, Vanderbilt University

[4]Department of Medicine, Vanderbilt University Medical Center

*Corresponding author

Contact information

Department of Pharmacology

Vanderbilt University

23rd Ave. S. at Pierce Ave.

Nashville, TN 37232-6600

Phone: (615)-875-7620

Email: qi.zhang@vanderbilt.edu

Summary (150 words)

The amyloid precursor protein (APP) has been extensively studied because of its relevance to Alzheimer's disease (AD). However, its membrane distribution and neuronal function remains unclear. Here, we generated an APP fusion protein with a pH-sensitive green fluorescent protein at its ectodomain and a pH-insensitive blue fluorescent protein at its cytosolic domain to measure surface and intracellular APP distributions and its cleavage events. This fusion protein, closely resembling endogenous APP, demonstrated a limited correlation between synaptic activities and APP trafficking at synapses and neurites. Inhibition of the three major secretases distinctly affected membrane APP distribution. Intriguingly, surface APP was inversely correlated to membrane cholesterol, a phenomenon involving APP's cholesterol-binding motif. Point mutation within this motif not only increased surface APP but also caused synaptic swelling when membrane cholesterol was reduced. Our results reveal previously unappreciated relationships between APP trafficking and processing and between membrane APP and cholesterol homeostasis at synapses.

Keywords

Alzheimer's disease, Amyloid precursor protein, Secretase, Trafficking, Proteolysis, Cholesterol, Synaptic Vesicle, Membrane, Exocytosis, Endocytosis

Introduction

Amyloid plaques, the hallmark of Alzheimer's disease (AD), are primarily comprised of β-amyloid peptides (Aβs). Aβs are proteolytic products of the amyloid precursor protein (APP), an integral membrane protein with a single transmembrane domain (Kang et al., 1987; Reinhard et al., 2005). Due to its linkage to AD, APP and its proteolytic processing have been investigated since the early 1980s (Hardy and Allsop, 1991). It has been well documented that APP is usually subject to one of two routes of proteolytic processing, amyloidogenic and nonamyloidogenic, catalyzed by three proteases known as the α-, β- and γ-secretases (αS, βS and γS) (**Figure 1A**) (Haass et al., 2012). In the amyloidogenic pathway, APP is first cleaved by βS in its membrane-proximal ectodomain to generate a large soluble protein (sAPPβ) and a membrane-bound C-terminal fragment (CTF) of 99 amino acid residues (C99). Subsequently, C99 is cleaved by γS within the transmembrane domain, yielding Aβs and a short intracellular C-terminal fragment (AICD). In the nonamyloidogenic pathway, APP is first cleaved by αS at an extracellular site just before the transmembrane domain to generate a longer soluble ectodomain (sAPPα) and a membrane-bound 83-residue CTF (C83). C83 is also cleaved by γS within the transmembrane domain, generating a shorter 30mer peptide (P3) and an identical AICD (Haass et al., 1992). Interestingly, membrane cholesterol enhances βS (von Arnim et al., 2008; Xiong et al., 2008) and γS (Grimm et al., 2008; Runz et al., 2002; Xiong et al., 2008) activities but has been reported to suppresses αS activity (Bodovitz and Klein, 1996; Kojro et al., 2001). Since APP's expression is ubiquitous, most studies on APP processing have been conducted in non-neuronal cells or cell lines (Chen et al., 2015; Sun and Roy, 2017) for reasons of technical practicality. In those cells, the majority of the APP is found in the

Golgi and trans Golgi network (TGN) and only a small portion is sorted to the plasma membrane (Kuentzel et al., 1993). Investigations using those cells revealed that αS cleaves APP in the plasma membrane, whereas both βS and γS cleave APP in endocytic compartments (Parvathy et al., 1999; Refolo et al., 1995), suggesting that APP's subcellular membrane localization determines its proteolytic fate.

While those studies have been revealing, they raised more questions that only studies using neurons from the central nervous system (CNS) can answer for the following eight reasons. Neurons are morphologically unique given their high polarity, extended axons and dendrites and specialized transcellular connections known as synapses, which means a complicated cellular membrane system unmatchable by any other cell types. Second, the distinct lipid composition of neuronal membrane and its electrophysiological properties have profound influence on membrane proteins like APP. Third, APP is reportedly enriched at synapses and found to be associated with synaptic vesicles at the presynaptic terminals (Groemer et al., 2011; Wilhelm et al., 2014). Fourth, some proposed APP functions, such as promoting axon outgrowth and synaptogenesis, have yet to be tested in neurons (Kamal et al., 2001; Priller et al., 2006; Wei et al., 2010). Fifth, APP expression, distribution, and cleavage are all reportedly associated with neuronal activity and its proteolytic products are also reported to modify neurotransmission reciprocally (Cirrito et al., 2008; Wang et al., 2017). Sixth, APP695 the most disease-relevant APP isoform, is predominantly expressed in neurons but not in glial cells or other non-neuronal cells (Rohan de Silva et al., 1997). Seventh, all three secretases that cleave APP are known to include functions that are unique to neurons, like modulating synaptic

transmission and plasticity (Wang et al., 2012). Finally, APP mutations associated with familial AD predominantly cause pathological changes in the CNS (De Strooper and Karran, 2016). We therefore sought to conduct studies of APP in live neurons.

To best deal with technical challenges such as cell type heterogeneity and morphological complexity imposed by CNS neurons, we conducted live cell imaging. Recent developments in functional fluorescent reporters enabled the use of fluorescence imaging for both qualitative and quantitative analyses of APP in live neurons. For example, by labeling APP and BACE-1 with two different fluorescent proteins or two complementary parts of one fluorescent protein, Roy and his colleagues revealed activity-dependent and independent convergence of these two proteins in different intracellular compartments in hippocampal neurons (Das et al., 2013; Das et al., 2015). Additionally, Groemer et al tagged APP's N-terminal with a pH-sensitive green fluorescence protein (i.e. pHluorin) to evaluate the coupling between APP trafficking and synaptic vesicle turnover (Groemer et al., 2011).

In the present study, we generated pH-APP-BFP2 by adding pH-insensitive BFP2 to pH-APP's C-terminal. We also co-expressed a pH-sensitive red fluorescence reporter selective for synaptic vesicles, Synaptophysin-pHTomato (SypHTm) (Li and Tsien, 2012), which enables us to evaluate the spatiotemporal correlations between APP and synaptic vesicles. We performed multichannel live cell imaging to investigate APP's subcellular distribution, trafficking, its association with synaptic transmission, the coupling between APP trafficking and cleavage, and its relationship to membrane cholesterol. Our results

not only revealed an intricate coupling between APP's trafficking and processing but also its involvement in membrane cholesterol homeostasis, especially at presynaptic terminals.

Results

Construction and characterization of a triple-fluorescence reporter system

We started with Groemer's pH-APP (gifted by the J. Klingauf lab) for several reasons. First, it is based on ratAPP695, matching our rat postnatal hippocampal culture. Secondly, its expression is driven by a human Synapsin 1 promoter (hpSynI), ensuring neuron-specific and moderate expression (Kügler et al., 2001). Thirdly, pHluorin was inserted near APP's N-terminal, right behind APP's short signaling peptide (SP), ensuring the same subcellular distribution pattern as native APP695 (Bauereiss et al., 2015; Groemer et al., 2011). Because intracellular membrane compartments like synaptic vesicles and lysosomes are often acidic (pH5.5~6.5) whereas extracellular pH is generally neutral (pH7.35), the pH-sensitive pHluorin located in APP's ectodomain exhibits an increase in fluorescence increase or a decrease during APP externalization or internalization respectively (Groemer et al., 2011). However, using pHluorin alone has some limits. First, it does not allow us to track intracellular APP since pHluorin is quenched in the acidic lumen. Second, N-terminal cleavage by αS or βS detaches pHluorin, yielding non-fluorescent CTFs. Third, a high concentration (e.g. 50 mM) of NH_4Cl is needed to unquench all intracellular APP for quantification (Groemer et al., 2011; Miesenbock et al., 1998). However, such high concentration NH_4Cl significantly alters neuronal membrane property and synaptic activity (Lazarenko et al., 2017), such that total APP and CTFs

cannot be continuously monitored while keeping neurons physiologically normal. We reasoned that adding a pH-insensitive fluorescent protein like BFP2 to APP's cytosolic domain (i.e. C-terminal) should address those issues because it provides an independent and persistent fluorescent signal for APP and CTFs. Previous studies have shown that an APP fusion protein with fluorescent proteins at both terminals behaves the same as endogenous APP. For example, Villegas et al showed that dual-tagged APPs (i.e. CFP-APP-YFP and FLAG-APP-Myc) were the same as endogenous APP in terms of intracellular distribution and transportation (Villegas et al., 2014). Hence, we attached BFP2 (gifted by Yulong Li) to pH-APP's C-terminal to generate pH-APP-BFP2. To independently visualize synapses and synaptic activity in the same neurons, we inserted Synaptophysin-pHTomato (SypHTm, also gifted by Yulong Li) (Li and Tsien, 2012) and a "self-cleavage" oligopeptide (T2A) (Osborn et al., 2005) in front of the pH-APP-BFP2 (**Figure 1A**). By so doing, the SypHTm will be co-expressed with pH-APP-BFP2 and post-translationally separated. Indeed, an immunocytochemistry test using Synaptotagmin I, a synaptic vesicle specific protein, confirmed that SypHTm was mostly synaptic whereas pH-APP-BFP2 was more diffused across the neurons (**Supplementary Figure 1**).

To visualize neurites and synapses with fluorescence microscopy, we used a modified transfection protocol (Jiang and Chen, 2006) to achieve 10-30% expression in synaptically mature hippocampal cultures (i.e. DIV12-18), yielding sparsely labeled neurons, neurites and synapses. Fluorescence images showed that pHTm was more punctated whereas BFP2 and pHluorin were more diffused in the neurites (**Figure 1B**), consistent with the notion that Syp is a synaptic vesicle-specific protein whereas APP is

not. We also observed that most pHTm puncta were overlapped with BFP2 and pHluorin (white arrowheads in **Figure 1B**) but not the other way around (cyan arrows in **Figure 1B**), suggesting APP and CTFs are more ubiquitously distributed across neurites than vesicular proteins. There were puncta with strong BFP2 and weak pHluorin fluorescence (blue arrowhead in **Figure 1B**), reflecting membrane compartments enriched with CTFs but not APP. Next, we asked if the membrane orientation of SypHTm and pH-APP-BFP2 was correct (i.e. pHTm and pHluorin should be located extracellularly and/or luminally). To do so, we applied 50mM NH_4Cl to deacidify all intracellular membrane compartments, followed by pH5.5 buffer to quench all pHTm or pHluorin (**Supplementary Movie 1**) (Lazarenko et al., 2017). We observed significant pHTm and pHluorin fluorescence increase and decrease during 50mM NH_4Cl and pH5.5 treatments respectively (**Figure 1B&C**), which demonstrates the luminal localization of pHTm and pHluorin and thus the correct transmembrane conformations of both fusion proteins. Expectedly, BFP2 fluorescence was very stable except for gradual decay as a result of photobleaching (**Figure 1C**). Hence, we can calculate the total pHluorin or pHTm fluorescence by subtracting the baseline fluorescence (at pH5.5) from the maximum fluorescence (at 50mM NH_4Cl), the surface/out pHluorin or pHTm fluorescence by subtracting the baseline fluorescence (at pH5.5) from the pretreatment fluorescence (at pH7.3), and the intracellular/in pHluorin or pHTm fluorescence by subtracting the pretreatment fluorescence (at pH7.3) from maximum fluorescence (at 50mM NH_4Cl) (**Figure 1C**). Unlike pHluorin, pHTm is only partially quenched at pH5.5, allowing us to identify expressing neurons, neurites and individual synapses without the use of NH_4Cl (Li and Tsien, 2012). However, due to the incomplete quenching, SypHTm experienced more

photobleaching at high magnification (e.g. 100x), causing slight overestimate of the surface fraction of SypHTm (the pretreatment fluorescence was always imaged first by definition and NH_4Cl application for total fluorescence was always the last (Lazarenko et al., 2017)). Notably, this issue was negligible at low magnification (e.g. 20x) due to significantly less illumination. We therefore used low magnification images and found that surface pHluorin fraction was significantly more than surface pHTm fraction while intracellular pHluorin fraction was significantly less (**Figure 1D**) at the synapses. However, outside the synapses there is little difference between pHluorin and pHTm, suggesting Syp is synaptic vesicle specific whereas APP is equally distributed in the surface and intracellular membrane (**Figure 1D**). At non-synaptic regions of the neurites, the trend remained but the difference was no longer statistically significant likely due to the lack of synaptic vesicles in neurite shafts. Hence, we conclude that SypHTm and pH-APP-BFP2 distributed independently, matching their endogenous counterparts.

Next, we asked if the dual-tagged pH-APP-BFP2 has the same distribution pattern in neuronal processes as endogenous APP. For reliable comparison, we performed fluorescent immunostaining for both endogenous APP and exogenously expressed pH-APP-BFP2 using an anti-APP antibody (recognizing APP's N-terminus) and an anti-GFP antibody (recognizing pHluorin) respectively. In addition, MAP2 immunostaining was used to identify dendrites, and Synapsin I immunostaining was used to identify synaptic boutons and axons bearing those boutons (**Figure 2A**). The amount of endogenous or exogenous APP in the synapses, axonal shafts, and dendritic shafts was normalized to total APP in the corresponding neurites. We found that endogenous APP and pH-APP-

BFP2 were very similar in terms of their distributions in axon, dendrite and synaptic boutons — more in synaptic boutons, less in dendritic shafts and the least in axon shafts (**Figure 2B**), clearly correlated to the total amount of surface and intracellular membranes in those subcellular structures.

We also asked if pH-APP-BFP2 was proteolytically processed as endogenous APP. Based on inhibitors' selectivity, potency and usage reported in the literature, we selected GI 254023X, βS inhibitor II (i.e. CAS 263563-09-3) and Compound E (i.e. CAS 209986-17-4) to block αS, βS and γS respectively. Using ELISA assays for sAPPα and Aβ40, we determined that 24-hour incubation was sufficient for the inhibitors to take effects (**Supplementary Figure 2**). Since αS and βS release APP's N-terminal ectodomain including pHluorin whereas γS releases the cytosolic C-terminal domain including BFP2, these secretase inhibitors should alter N *vs.* C terminal ratio or total pHluorin *vs.* BFP2 ratio. For endogenous APP, we performed fluorescence immunostaining using antibodies selective for APP's N- and C-terminals (22C11 and Y188 respectively) (**Figure 2C**). As expected, immunofluorescence analyses showed that both αS and βS inhibition increased the N/C ratio for endogenous APP at synaptic boutons marked by Syp whereas γS inhibition decreased the ratio (**Figure 2D**). For pH-APP-BFP2, we conducted live cell imaging to measure total pHluorin *vs.* BFP2 ratio while using the SypHTm signal to identify synaptic boutons (**Figure 2E**). Again, live cell imaging showed that the changes of this ratio was very similar to the changes of N/C ratio from the immunostaining of endogenous APP (**Figure 2F**). Notably, the fluorescent signals from the live cell imaging are more discrete than those from immunostaining, mostly owning to the neuron-specific

gene expression, which makes the difference among the four groups more significant. This is further supported by the results from non-synaptic regions, in which the total pHluorin vs. BFP2 ratios are very similar to those of synaptic regions (**Supplementary Figure 3**). Therefore, all our comparisons between endogenous APP and exogenous pH-APP-BFP2 demonstrate that despite the extra fluorescent proteins at both ends, pH-APP-BFP2 exhibits the same membrane orientation, subcellular distribution and proteolytic processing as those of endogenous APP.

APP and synaptic activity

A large body of evidence suggests that APP subcellular trafficking and surface turnover are influenced by neuronal activity, linking APP abnormalities to synaptic dysfunction commonly found in animal models and preclinical AD patients (Selkoe and Hardy, 2016; Toh and Gleeson, 2016). Taking advantage of the fast response of pHluorin fluorescence and the high temporal resolution of optical imaging, we asked if APP trafficking between synapses or between surface and intracellular membranes was associated with acute neuronal activity changes, a question that cannot be readily addressed using conventional biochemical approaches. First, we examined if the mobility of APP and/or CTFs was affected by synaptic activity. We applied two different stimuli (a 1-minute 10-Hz electric field stimulation and a 1-minute 90-mM K^+ perfusion) each separated by a 1-minute resting period long enough for the synapses to recover. Since pHluorin fluorescence only represented surface APP at pH7.35 bath solution and could be altered by stimulation-induced exo-/endocytosis, we imaged BFP2 to track the movement of all APP and its C-terminal fragments (**Figure 3A** and **Supplementary Movie 2**). Again,

SypHTm was used to mark the positions of synaptic boutons in transfected neurons. The comparison between the sample kymographs of pHTm and BFP2 illustrates the random behaviors of BFP2 puncta, i.e. stationary or mobile, anterograde or retrograde, and toward or away from nearby synaptic boutons (**Figure 3B**). When plotted against time, neither the velocity (**Figure 3C**) nor the distance from the nearest synapse (**Figure 3D**) of the moving BFP2 puncta exhibited any significant difference between stimulation or resting periods, suggesting that APP and/or CTFs move rather randomly instead of directionally (with respect to the synapses) and are not affected by acute activity change.

We next asked if APP's turnover between surface and intracellular membranes is correlated to activity-associated synaptic vesicle exo-/endocytosis. To do so, we utilized SypHTm fluorescence change as a measure for synaptic vesicle turnover (Li and Tsien, 2012). If APP, like Syp, was selectively associated with synaptic vesicles, SypHTm and pHluorin fluorescence should exhibit correlated changes during stimulation. Again, we applied an intense stimulation, 90 mM K^+, and simultaneously measured the pHTm and pHluorin fluorescence changes at the same synapses. While we observed an increase of pHluorin fluorescence at synaptic boutons, neither the amount nor the rate of change was correlated to those of the pHTm fluorescence (**Figure 3E&F**). Furthermore, we did not observe consistent correlations for the total, surface or intracellular pHluorin and pHTm fluorescence intensities at synaptic boutons (**Supplementary Figure 4**). These data again suggest that, unlike Syp, synaptic APP is not proportional to synaptic bouton size or synaptic vesicle population, and its surface-intracellular turnover is affected but not directly mediated by synaptic vesicle turnover.

APP proteolysis and surface turnover

As different secretases locate and cleave APP in different membrane compartments (O'Brien and Wong, 2011; Selkoe and Hardy, 2016). Moreover, inhibition of different secretase(s) can affect APP distribution as well. Additionally, uncleaved APP or CTFs may relocate to other membranes, causing functional changes. Since pHluorin and BFP2 signals allow us to estimate N- and C-terminal cleavage respectively, we investigated whether and how inhibition of αS, βS and/or γS alters APP distribution. We applied the three ELISA-validated inhibitors (**Supplementary Figure 2**) separately or in combination, and quantified surface, intracellular and total pHluorin as well as BFP2. For comparison, we calculated the ratios such as that for intracellular *vs.* total pHluorin in both synaptic and non-synaptic regions. For easy visualization, we converted those ratiometric values to color-coded charts (**Figure 4**) supplied with corresponding scatter plots of the background subtracted fluorescence values (**Supplementary Figure 5** and **6**).

As expected, αS inhibition doubled the total pHluorin *vs.* BFP2 ratio (from 0.33 ± 0.02 to 0.66 ± 0.04) at synaptic boutons (**Figure 4A** and **Supplementary Figure 5D**&**E**), consistent with the notion that αS cleavage is the major APP N-terminal cleavage and βS alone is not sufficient to process the excessive APP. Instead of remaining in the plasma membrane, the uncleaved APP was accumulated intracellularly, as shown by a decrease of surface APP fraction and an increase of intracellular fraction. This holds true in non-synaptic regions as well (**Figure 4B** and **Supplementary Figure 6D**&**E**), indicating that the surface APP level is more strictly controlled than the intracellular level. Notably, there

were similar changes in surface and intracellular pHTm distributions although much smaller (**Supplementary Figure 5F**). As expected, βS inhibition caused less of an increase in the total pHluorin *vs.* BFP2 ratio (~55%, from 0.33 ± 0.02 to 0.51 ± 0.03) than αS inhibition did, and uncleaved APP again accumulated intracellularly at synaptic boutons (**Figure 4, Supplementary Figure 5G**&**H** and **6G**&**H**). Changes in surface and intracellular pHTm (**Supplementary Figure 5I** and **6I**) were similar to those of αS inhibition and in the same direction as those of pHluorin. γS inhibition expectedly reduced the total pHluorin *vs.* BFP2 ratio to 33% (from 0.33 ± 0.02 to 0.11 ± 0.01) due to a significant increase of uncleaved CTFs (**Figure 4, Supplementary Figure 5J**&**K** and **6J**&**K**). Intriguingly, there was a significant increase of surface APP fraction (i.e. increase of surface vs total pHluorin ratio). Even more interesting is a greater increase of surface pHTm fraction (**Supplementary Figure 5L** and **6L**), suggesting an imbalance of synaptic vesicle release and retrieval when γS was inhibited. While such an imbalance may be accountable for increased surface APP at synaptic boutons, it cannot explain the same increase at non-synaptic regions lacking synaptic vesicles. An alternative explanation is that other γS substrates, CTFs, or even membrane lipids are affected by γS inhibition, resulting in direct and consequently alter membrane APP trafficking.

Next, we applied different combinations of secretase inhibitors and tested their effects on APP trafficking and synaptic vesicle turnover (**Figure 4** and **Supplementary Figure 5**&**6**). The inhibition of both αS and γS caused a greater increase in APP than in CTF (i.e. ~55% increase of total pHluorin *vs.* BFP2 ratio), and, consistently, most uncleaved APP remained intracellular (**Figure 4**, **Supplementary Figure 5M**&**N** and **6M**&**N**). Additionally,

the pHTm distribution changed in a manner similar to that of APP (**Supplementary Figure 5O** and **6O**), i.e. there was more intracellular SypHTm. The inhibition of both βS and γS caused a greater increase in CTF than APP (i.e. ~39% decrease in total pHluorin *vs.* BFP2 ratio), and most uncleaved APP again remained intracellular (**Figure 4**, **Supplementary Figure 5P**&**Q** and **6P**&**Q**). Again, there was a small change in pHTm distribution, in the same direction as that of APP (**Supplementary Figure 5R** and **6R**), i.e. there was more intracellular localization of SypHTm. Inhibition of both αS and βS also caused more increase in APP than CTF, (i.e. ~52% increase in total pHluorin *vs.* BFP2 ratio) (**Supplementary Figure 5T**&**6T**), and uncleaved APP again accumulated in the intracellular compartments (**Figure 4**, **Supplementary Figure 5S** and **6S**). The inhibition of three major secretases caused a greater CTF increase than APP increase, (i.e. ~36% decrease in total pHluorin *vs.* BFP2 ratio) (**Supplementary Figure 5W**&**6W**). More interestingly, there was much greater increase of surface APP than that of intracellular APP (**Figure 4**), accompanied by a similar change in SypHTm distribution (**Supplementary Figure 5X** and **6X**). Collectively, these results implicate alternative N-terminal cleavage mechanism(s), a close association between APP processing and surface trafficking, strict control of surface APP level, and a loose association between APP surface turnover and synaptic vesicle recycling.

Neuronal surface membrane cholesterol and APP distribution

The strict control of surface membrane APP and its disruption by γS inhibition prompted us to identify membrane factor(s) that can link the two together. On one hand, it is well known that all three secretases are sensitive to cholesterol in cell membranes. On the

other hand, recent structural studies using nuclear magnetic resonance spectroscopy (NMR) revealed a cholesterol-binding motif, implicating a specific interaction between cholesterol and APP in neuronal membrane (Barrett et al., 2012; Beel et al., 2008; Beel et al., 2010). This is interesting not only because neuronal membranes have much higher cholesterol content than most other types of cells in the human body (Pfisterer et al., 2011), but also because cholesterol seems to be closely linked to AD. First, ApoE4, the highest genetic risk factor for late-onset AD (a.k.a. sporadic AD), leads to a reduced cholesterol supply to neurons compared to the AD-protective or benign ApoE2&3 variants (Mahley, 2016). Second, when cholesterol transportation to the plasma membrane is disrupted by mutations like NPC1 (found in Niemann-Pick Type C1 disease) (Blanchette-Mackie, 2000), AD-like histopathologies, including abnormal Aβ metabolism, neurofibrillary tangles and neurodegeneration, appear. Third, increasing membrane cholesterol shifts APP processing from the non-amyloidogenic mode to amyloidogenic by suppressing αS (Bodovitz and Klein, 1996; Harris et al., 2009; Kojro et al., 2001) and promoting βS and γS (Kim et al., 2016; Liu et al., 2009). Fourth, APP and ApoE reciprocally modulate each other's expression (Huang et al., 2017; Liu et al., 2007; Nhan et al., 2015). Fifth, cholesterol and ApoE4 reportedly affects the clearance of Aβ aggregates. Sixth, cholesterol is essential for exo-/endocytosis of synaptic vesicles (Korade and Kenworthy, 2008). Seventh, age-related loss of membrane cholesterol is often accompanied by synaptic dysfunction during the preclinical stage of AD (Egawa et al., 2016).

Hence, we examined how synaptic APP processing and trafficking change upon membrane cholesterol reduction. We incubated hippocampal cultures with 1-mM MβCD (methyl-β-cyclodextrin) for 90 minutes, which caused a moderate (~10%) reduction of neuronal membrane cholesterol without detectable membrane damage or morphological change (**Supplementary Figure 7**). The most visible change we observed was a significant reduction of total pHluorin fluorescence (**Figure 5A-D**), consistent with an increase in αS cleavage caused by lower membrane cholesterol promotes. Notably, the reduction of surface pHluorin was less than that of intracellular pHluorin, leading to a relative increase in the surface APP fraction (**Figure 5E**). Intriguingly, there were similar changes in total and surface pHTm signals although less significant (**Figure 5F**&**G**). We next investigated whether the increase in surface APP fraction was indirectly caused by cholesterol-related change in secretase activity? For αS, it mostly cleaves cell surface APP (**Figure 4** and **Supplementary Figure 5D**&**6D**), MβCD-induced potentiation of αS could not be responsible for the increase of surface APP fraction. For βS, its suppression caused by MβCD is also unlikely accountable for the increase of APP surface fraction increase because our previous results (**Figure 4A** and **Supplementary Figure 5G**) showed that βS inhibition resulted in a reduction instead of an increase in the surface APP fraction. For γS, while its activity would have been reduced by membrane cholesterol loss, no increase in BFP2 fluorescence (**Figure 5C**&**D**) suggests that our mild MβCD treatment was insufficient to suppress γS. Therefore, it is likely that MβCD-snduced surface APP fraction increase was different from that of γS inhibition. Collectively, altered secretase activity upon the MβCD treatment did not appear to be account for the increased surface fraction of APP.

By combining MβCD and γS inhibitor treatments, we further tested if their effect on surface APP was additive. The total pHluorin signal was reduced to the same degree as MβCD alone (**Figure 5B**), and the BFP2 signal was increased by the addition of the γS inhibitor (**Figure 5C**). As such, the total pHluorin *vs.* BFP2 ratio reduced at similar degree as that of γS inhibitor (unpaired two-tailed *t*-test, $p = 0.6324$) and more than that of MβCD alone (unpaired two-tailed *t*-test, $p = 0.0140$) (**Figure 5D**), suggesting MβCD alone does not completely block γS activity. Analysis of the surface pHluorin fraction showed that the increase in surface APP was more than that by γS inhibition alone but no more than that by MβCD alone (**Figure 5E**). Moreover, the combined treatment caused a greater decrease of total SypHTm decrease (**Figure 5F**) and a higher surface SypHTm fraction than by MβCD or γS inhibitor alone (**Figure 5G**), which was similar to what we previously observed (**Supplementary Figure 5L**&**6L**). These data further suggest that the MβCD treatment had limited impact on γS activity and thus acted on surface APP distribution through mechanism(s) different from γS cleavage.

APP's cholesterol-binding ability affects its surface distribution

If membrane cholesterol modulates APP surface distribution independent of the three major secretases, does that involve a direct interaction between APP and cholesterol? In fact, a cholesterol-binding motif in APP has been identified recently based on NMR studies (Barrett et al., 2012; Beel et al., 2008; Beel et al., 2010; Song et al., 2013), which has yet to be physiologically validated. To test that, we introduced a point mutation (I703A) into SypHTm:T2A:pH-APP-BFP2. This amino acid residue was essential for cholesterol-

binding (Barrett et al., 2012) and distant enough from the cleavage sites for the three major secretases. We expressed this mutant as well as the wild type control in cultured neurons (**Figure 6A**). Again, we focused on SypHTm-marked synaptic boutons where APP changes occurred the most. We determined that the γS cleavage was not affected by the mutation: the mean value of BFP2 fluorescence (870.03 ± 78.124 a.u. for WT, 1075.10 ± 111.77 a.u. for I703A) was not significantly altered (two-tailed unpaired t-test, p = 0.1248). It appears that α- and β-cleavage are also unchanged: the mean total pHluorin value of the mutant is 216.65 ± 21.238 a.u., which is not significantly different from the wild type's value of 187.86 ± 13.128 a.u. (two-tailed unpaired t-test, p = 0.2329). However, I703A caused a significant increase of surface APP fraction (**Figure 6B**) with little change in surface SypHTm fraction (**Figure 6C**). This suggests that APP-cholesterol binding either prevents APP surface-localization or promotes its internalization, and it is independent of synaptic vesicle turnover, which is again different from that of γS inhibition.

Next, we asked if the mutation-associated increase can be augmented by inhibiting γS. As expected, the application of the γS inhibitor significantly decreased total pHluorin *vs.* BFP2 ratio in both wildtype and I703A (**Figure 6D**), suggesting the mutant was as equally cleavable by γS as the wildtype. While the γS inhibitor was able to increase surface APP fraction in the wildtype, it failed to do so for I703A (**Figure 6E**). This result resembles that of the combination of MβCD and γS inhibitor, and it was unlikely due to a ceiling effect because overall APP(I703A) was also decreased by MβCD and the surface APP(I703A) was decreased less than the intracellular APP. This set of results suggest that a direct interaction between membrane cholesterol and APP is involved in the regulation of

synaptic surface APP and that γS is unlikely to be directly involved in this regulation. Furthermore, their resemblance to MβCD results indicates that cholesterol is a negative regulator for APP surface localization.

APP is involved in synaptic membrane cholesterol homeostasis.

Since cholesterol is critical for neuronal membrane integrity (Egawa et al., 2016; Korade and Kenworthy, 2008; Sebastião et al., 2013) and functionally essential for the origination as well as the recycling of synaptic vesicles (Dason et al., 2014; Pfrieger, 2003), we set to test the functional significance of APP's cholesterol-binding and surface distribution for presynaptic terminals. To simulate neuronal membrane cholesterol reduction during aging (Wood et al., 2011; Wood et al., 2002), we again used the mild MβCD treatment (1 mM for 90 min) in cultures expressing wild type or I703A APP. We found that the MβCD treatment caused significant swelling of synaptic boutons (i.e. SypHTm puncta) in mutant but not wildtype-expressing neurons (**Figure 7A**), which was confirmed by a significant increase in the area of SypHTm puncta (**Figure 7B**). Intriguingly, MβCD significantly increased the surface APP fraction at synaptic boutons in both wildtype and I703A (**Figure 7C**), suggesting that membrane cholesterol reduction was still able to drive the surface APP increase regardless the point mutation. Similarly, MβCD also increased surface SypHTm at synaptic boutons in both cases (**Figure 7D**).

To understand how the synaptic swelling occurred and how the mutated APP was involved, we set up time-lapse imaging for pHluorin, BFP2 and pHTm during the MβCD treatment. As described before, I703A had brighter pHluorin and pHTm fluorescence than

the wild type to start with. During the course of the MβCD treatment, pHluorin fluorescence was significantly increased further at synaptic boutons expressing both wildtype and I703A (**Figure 7E**). However, the increase in wild type was relatively small and mostly occurred at the beginning of the MβCD treatment whereas the increase in I703A was significantly large and continued through the whole treatment, matching the abnormal swelling of synaptic boutons. In contrast, BFP2 fluorescence remained the same in both cases, indicating either unchanged γS activity or APP/CTF degradation by other means (**Figure 7F**). The increase of surface APP at synaptic boutons was unlikely caused by excessive exocytosis of synaptic vesicles as pHTm showed no further increase in both wildtype and I703A groups during MβCD treatment (**Figure 7G**). Together, this set of experiments suggests that, when membrane cholesterol was reduced, disruption of cholesterol-binding unleashed the restriction on APP surfacing, which was independent of synaptic vesicle turnover and was detrimental to synaptic boutons.

Discussion

Previous studies on subcellular APP distribution were mostly performed in cell lines and with biochemical methods such as surface biotinylation and western blot. This may not be directly applicable to neurons due to their morphological complexity and functional uniqueness. Our multi-color imaging with a dual- fluorescence APP reporter (i.e. pH-APP-BFP2) and a synaptic vesicle reporter (i.e. SypHTm) offers sufficient spatiotemporal resolution to address these challenges, given that the APP reporter very much resembles endogenous APP. Furthermore, an APP with protein markers fused to both terminals has

been developed and used in various types of cells before (Villegas et al., 2014). While the dual-fluorescence reporter allows us to measure surface and intracellular APP and N/C-terminal cleavage, it cannot distinguish non-amyloidogenic and amyloidogenic cleavages. It is possible that a spectrally separable fluorophore or a conjugation site can be added in between the αS and βS cleavage to enable the distinction of C83 (BFP2 alone) and C99 (BFP2 and the third fluorophore).

Due to its abundance at presynaptic terminals (Wilhelm et al., 2014), APP is believed to be functionally involved in synaptic vesicles exo-/endocytosis and thus neurotransmission (Fanutza et al., 2015). However, Groemer et al demonstrated that only about 10% APP was recycled with synaptic vesicles (Groemer et al., 2011). A more recent study showed that APP is enriched in the presynaptic active zone but not free synaptic vesicles (Laßek et al., 2013). While our data showed that APP did surface during stimulation, the rate was much slower than that of Syp, a synaptic vesicle protein. Additionally, the surface fraction of APP at synaptic boutons was significantly more than that of Syp. One possibility is that APP is localized to the presynaptic active zone and endosome/lysosome membranes, but not to synaptic vesicles. Hence, only prolonged stimulation that forced vesicle regeneration from endosomes was able to move a limited fraction of intracellular APP to the presynaptic surface. Alternatively, it could reflect a tightly coupled vesicle retrieval mode (Zhang et al., 2009) in which the surfacing and internalization of vesicular APP were balanced at the beginning of stimulation, but that was eventually unbalanced by extensive vesicle release. In addition, a continuous decay of pHluorin fluorescence after stimulation stopped suggests that the externalized APP has to be removed to keep the surface APP

level steady. Furthermore, we examined the lateral movement of BFP2 puncta, likely cargo vesicles carrying APP or CTF, as they were not confined to synaptic boutons and showed no pHluorin intensity changes during stimulation. We could not distinguish between APP or CTF because the pHluorin fluorescence of the former was quenched by the acidic luminal pH. Nevertheless, the lack of correlation between BFP2 mobility and neuronal activity or between its position and synaptic boutons suggests that the trafficking of APP and/or CTF in neurites is unlikely to be regulated by neuronal activity. In light of the recent imaging studies of APP and BACE-1 (Das et al., 2013), we speculate that the activity-dependent proteolysis of APP/CTF mostly occurred at somatodendritic regions whereas APP/CTF at the distal synaptic boutons behaves differently. Combining our use of pH-APP-BFP2 with the employment of red fluorescent protein-tagged secretases like BACE-1 will be useful in addressing those questions.

Reducing Aβ production has been one of the major therapeutic strategies tested clinically. However, little is known about how secretase inhibition will impact APP's surface and intracellular distribution in neurites and synapses. On one hand, it is well documented that different secretases cleave APP/CTF in different membrane compartments and that their activities are greatly affected by the environment such as membrane cholesterol concentration and pH (Haass et al., 2012). On the other hand, the localization of APP or CTF is essential for specific functions they reportedly execute (Muller and Zheng, 2012). Therefore, secretase inhibition can change APP distribution and function. Our findings not only support this notion but also suggest that neuronal surface membrane APP is tightly controlled except after γS inhibition. Notably, application of γS inhibitor alone or in

combination with other inhibitors also significantly increased surface SypHTm, suggesting a side effect on synaptic vesicle turnover and likely synaptic transmission. However, it is unlikely that the surfacing of vesicular membrane components was the major cause of surface APP increase because (1) the later also occurred at neurite shafts, (2) its increase was much more than that of surface SypHTm, and (3) APP might be less abundant in synaptic vesicles than previously thought (Groemer et al., 2011; Laßek et al., 2013). We speculate that the excessive CTF after γS inhibition might contribute to the unexpected increase in surface APP caused by heterodimerization with APP (discussed in detail later).

Cholesterol has been suspected as a pathological factor in AD, although it remains unclear whether it is cholesterol in lipoproteins, in cell membranes, or in both that is responsible (Burns et al., 2006). For example, cholesterol has been related to Aβ clearance via low density lipoprotein receptor-related protein 1 (LRP1) (Shinohara et al., 2017) and to Aβ production via altering secretase activity (Cam and Bu, 2006). The fact that our moderate MβCD treatment significantly reduced the total pHluorin fluorescence is in good agreement with the latter idea, especially because αS cleavage was greatly promoted by lowering the plasma membrane cholesterol. With the overall APP reduction, we discovered that the surface fraction of APP was relatively increased, likely due to reduced internalization. When we combined MβCD with the γS inhibitor, we found no further increase in surface APP fraction, pointing to a dominant role of membrane cholesterol in determining the surface APP. Furthermore, the increase of surface APP is not directly caused by a change in γS activity because the I703A mutation increased surface APP without affecting γS cleavage. However, it is possible that γS, by regulating

membrane cholesterol, indirectly contributes to the increase of surface APP (Tamboli et al., 2008), which is consistent with the dominance of MβCD and the I703A mutation over γS inhibitor in increasing surface APP.

Another explanation for the MβCD-associated increase in the surface APP fraction is that reducing membrane cholesterol interrupts the retrieval of synaptic vesicles (Dason et al., 2010, 2014), which is supported by the increase of surface SypHTm. In fact, a more recent study demonstrated concentration-dependent differences in the effects of MβCD on the synapse (Yue and Xu, 2015). Mild cholesterol reduction impaired endocytosis whereas severe depletion impaired both endo- and exocytosis. However, in our tests, the increase of surface APP did not match that of surface SypHTm proportionally and it is questionable whether synaptic vesicles had enough APP to be accountable for the increase. Cossec et al. also found that cholesterol depletion increased the level of surface APP, consistent with our results that increasing plasma membrane cholesterol decreases the surface fraction of APP via clathrin-mediated endocytosis (CME) (Cossec et al., 2010). If so, the explanation for our data can involve more than synaptic vesicle endocytosis as CME is essential for many other forms of surface membrane internalization. For example, the well-established LRP1-mediated endocytosis of APP is via CME as well (Herr et al., 2017). Reduced clustering in lipid rafts is also a potential contributor to reduced endocytosis (Schneider et al., 2008). It will be interesting to see if disabling LRP1 (e.g. knockdown) or the more ubiquitous dynamin (e.g. Dynasore, a membrane-permeable dynamin inhibitor) will affect this MβCD-associated surface APP fraction increase.

Recently, a structure-based study revealed a cholesterol-binding motif made of the C-terminal of APP's ectodomain and the N-terminal of its transmembrane domain (Barrett et al., 2012), supporting the notion that APP directly and specifically interacts with cholesterol in cell membranes. Interestingly, overexpression of APP was recently found to decrease neuronal activity via reducing cholesterol turnover, and APP's transmembrane domain containing part of the cholesterol binding motif is required for this effect (Pierrot et al., 2013). Our tests using the APP point mutation confirm that this cholesterol-binding capability is physiologically significant. The fact that the mutation increased surface distribution without changing SypHTm distribution or secretase cleavage suggests that cholesterol-binding either facilitates APP internalization or prevents its surfacing independent of synaptic vesicle turnover. Adding a γS inhibitor failed to increase its surface fraction, further confirming that cholesterol directly regulates APP surface distribution. More importantly, the overexpressed APP mutant rendered the mild MβCD treatment destructive to neurons, i.e. causing severe swelling of synaptic boutons. The synaptic swelling was accompanied by massive surfacing of mutated APP, indicating dysregulation of APP and lipid membranes. The fact that mutant APP showed an increase in surface localization during MβCD treatment implies that APP surfacing is driven by membrane cholesterol but may not require direct binding between APP and cholesterol. Instead, it may be the APP internalization that requires direct cholesterol binding, which is consistent with the net increase of surface APP caused by the mutation without other treatments.

The effect of the APP mutant was seemingly dominant negative as endogenous wildtype APP was still being expressed. The explanation for that may reside in APP's homodimerization or heterodimerization with CTF. Intriguingly, the cholesterol-binding motif partially overlaps with the proposed dimerization motif (Barrett et al., 2012; Yan et al., 2017), and competition between cholesterol-binding and APP/CTF-dimerization has been observed in a biophysical study (Song et al., 2013). Hence, it is possible that the mutant dimerized with wildtype APP or CTF and rendered them insensitive to membrane cholesterol change. Furthermore, the dimerization may also be accountable for the increase of surface APP after γS inhibition. Interestingly, Eggert et al. demonstrated that APP homodimers are preferentially located in the endosomes in HeLa cells, and that induced homodimerization reduces surface APP fraction (Eggert et al., 2017a). We postulate that the competition with intracellularly accumulated CTFs after γS inhibition reduced APP homodimers and allowed more APP to reach the plasma membrane. Eggert et al. also showed that APP homodimerization reduced co-transport with the sorting protein, SorLA. Notably, the SorLA binding sites are in the APP N-terminus/ectodomain (Andersen et al., 2006), which has been cleaved off of the CTFs. Therefore, APP/CTF heterodimers are likely to bind SorLA and potentially other sorting and transport proteins, thus escaping from the endosomes and ultimately reaching the plasma membrane in higher concentrations than are otherwise possible. An additional molecular explanation Eggert et al. proposed was that APP dimerization blocks LRP1 binding. Unlike SorLA, LRP1 binds to the YENPTY motif in the cytoplasmic domain of APP (Pietrzik et al., 2002) via the adaptor protein FE65 (Pietrzik et al., 2002; Pietrzik et al., 2004). Because the cytoplasmic domain is intact in the CTFs, APP/CTF heterodimers can be as resistant to

LRP1 binding as APP homodimers. Long term inhibition of LRP1 binding to APP in cell lines (Ulery et al., 2000) and knocking out LRP1 in primary neurons (Herr et al., 2017) both resulted in drastic increases in APP surface fraction and production of sAPPα. If γS inhibition increases the surface fraction of APP through promotion of heterodimerization of APP and CTF, it logically follows that αS or βS inhibition would decrease the surface fraction by increasing full length APP and decreasing the production of CTFs, which is in fact what we observe (**Figure 4**). The further increase of surface APP by the combination of all three secretase inhibitors was seemingly contradictory since a higher total pHluorin *vs.* BFP2 ratio indicated more holo-APP than that of γS inhibitor alone (**Supplementary Figure 5K**&**W**). However, a comparison to αS&βS inhibition (**Supplementary Figure 5T**&**W**) suggests that there was also significantly more CTF after inhibiting all three secretases. It is possible that other N-terminal cleavage events such as η-secretase cleavage (Willem et al., 2015) took over and generated more alternative CTFs equally capable of forming heterodimers with extra APP. Hence, it will be interesting to test the formation of APP-CTF heterodimer and the impact of CTF overexpression on APP surface distribution, especially with γS inhibition, membrane cholesterol reduction, and/or with an APP point mutation. As fluorescent methods like FRET have been developed to study APP/CTF dimerization in cells (Yan et al., 2017), it is possible to incorporate such an assay using spectrally compatible fluorophores.

Our results with the APP mutant support the notions that APP is essential for maintaining cholesterol homeostasis and for the integrity of presynaptic membranes, which points to a less appreciated link between APP and APOE (Gamba et al., 2012). In addition, the

association between APP and membrane cholesterol may also help to reconcile various cellular functions proposed for APP, because membrane cholesterol, especially via membrane microdomains, has broad physiological impacts on various cellular processes like transmembrane signaling and membrane trafficking (Simons and Gerl, 2010; Wood et al., 2011). We postulate that APP is a cholesterol sensor for cholesterol homeostasis between presynaptic surface and intracellular membranes. It is well documented that presynaptic terminals, especially the synaptic vesicles they contain, have a much higher concentration of cholesterol in comparison to that of the plasma membrane (Takamori et al., 2006), whereas other intracellular organelles like endosomes have far less membrane cholesterol than the plasma membrane. This means that activity-evoked vesicle release will lead to a substantial increase of cholesterol in the surface membrane and a correspondingly profound decrease in vesicular and other intracellular membrane at the presynaptic terminals. Intriguingly, APP resembles the well-studied sterol regulatory element binding protein (SREBP) (Ebinu and Yankner, 2002) in several aspects including intracellular membrane localization, cholesterol-sensitivity, cleavage by regulated intramembrane proteolysis, and the function of their proteolytic products (i.e. transcription factor for cholesterol metabolism genes). Based on our observation about its surfacing in relationship to activity, γ-secretase inhibition, MβCD and its own cholesterol-binding motif, we further propose that APP can be a multifunctional player in retrieving surfaced membrane cholesterol, balancing intracellular membrane turnover and sensing endosomal cholesterol sensing, all of which agree well with APP's abundance in both surface and intracellular membrane sections and at presynaptic terminals. In addition, the mutual regulation between APP and LRP1 (Eggert et al., 2017b; Wagner and Pietrzik,

2012) also supports this idea. While our study demonstrates the physiological relevance of APP-cholesterol binding and the functional significance of APP's cholesterol-binding motif, it also raises many interesting questions about the relationship between membrane cholesterol, APP and secretases. With the increasing capabilities of fluorescent microscopy, the time seems ripe to test these questions in CNS neurons *in vitro* or even *in vivo*. With the help of optogenetics, these questions can and should be put into the context of synaptic activity and the neuronal network, which will not only reveal the intrinsic function of APP but also its pathological relevance to AD.

Acknowledgements

We thank R.M. Lazarenko and K. E. Kitko for technical help and sharing cell cultures. We thank K.P.M. Currie for comments and discussions. The pHluorin-APP was generously provided by J. Klingauf lab. We thank all members of the Zhang laboratory for their support. This work is funded by the National Institutes of Health (OD00876101 and NS094738 to Q.Z., and AG056147 to C.R.S.).

Author Contributions

C.E. DelBove and Q. Zhang conceived this project, designed experiments, analyzed the data and wrote the manuscript. C.E. DelBove conducted all experiments, with one exception. C.E. Strothman conducted SypHTm and pH-APP-BFP2 imaging with acute application of 90 K. C.E. DelBove, C.R. Sanders and Q. Zhang conceived and designed

the APP mutation experiments. H. Huang generated the APP point mutations. We thank X. Deng for experimental help, and all Zhang laboratory members for discussion.

Declaration of Interests

All authors declare no competing financial interests.

References

Andersen, O.M., Schmidt, V., Spoelgen, R., Gliemann, J., Behlke, J., Galatis, D., McKinstry, W.J., Parker, M.W., Masters, C.L., Hyman, B.T.*, et al.* (2006). Molecular Dissection of the Interaction between Amyloid Precursor Protein and Its Neuronal Trafficking Receptor SorLA/LR11†. Biochemistry *45*, 2618-2628.

Barrett, P.J., Song, Y., Van Horn, W.D., Hustedt, E.J., Schafer, J.M., Hadziselimovic, A., Beel, A.J., and Sanders, C.R. (2012). The amyloid precursor protein has a flexible transmembrane domain and binds cholesterol. Science *336*, 1168-1171.

Bauereiss, A., Welzel, O., Jung, J., Grosse-Holz, S., Lelental, N., Lewczuk, P., Wenzel, E.M., Kornhuber, J., and Groemer, T.W. (2015). Surface Trafficking of APP and BACE in Live Cells. Traffic *16*, 655-675.

Beel, A.J., Mobley, C.K., Kim, H.J., Tian, F., Hadziselimovic, A., Jap, B., Prestegard, J.H., and Sanders, C.R. (2008). Structural Studies of the Transmembrane C-Terminal Domain of the Amyloid Precursor Protein (APP): Does APP Function as a Cholesterol Sensor?†‡. Biochemistry *47*, 9428-9446.

Beel, A.J., Sakakura, M., Barrett, P.J., and Sanders, C.R. (2010). Direct binding of cholesterol to the amyloid precursor protein: An important interaction in lipid–Alzheimer's disease relationships? Biochimica et Biophysica Acta (BBA) - Molecular and Cell Biology of Lipids *1801*, 975-982.

Blanchette-Mackie, E.J. (2000). Intracellular cholesterol trafficking: role of the NPC1 protein. Biochimica et Biophysica Acta (BBA) - Molecular and Cell Biology of Lipids *1486*, 171-183.

Bodovitz, S., and Klein, W.L. (1996). Cholesterol modulates alpha-secretase cleavage of amyloid precursor protein. J Biol Chem *271*, 4436-4440.

Buades, A., Coll, B., and Morel, J.-M. (2011). Non-Local Means Denoising. Image Processing On Line *1*.

Burns, M.P., Igbavboa, U., Wang, L., Wood, W.G., and Duff, K. (2006). Cholesterol distribution, not total levels, correlate with altered amyloid precursor, protein processing in statin-treated mice. Neuromolecular Medicine *8*, 319-328.

Cam, J.A., and Bu, G. (2006). Modulation of beta-amyloid precursor protein trafficking and processing by the low density lipoprotein receptor family. Mol Neurodegener *1*, 8.

Chen, A.C., Kim, S., Shepardson, N., Patel, S., Hong, S., and Selkoe, D.J. (2015). Physical and functional interaction between the alpha- and gamma-secretases: A new model of regulated intramembrane proteolysis. Journal of Cell Biology *211*, 1157-1176.
Cirrito, J.R., Kang, J.-E., Lee, J., Stewart, F.R., Verges, D.K., Silverio, L.M., Bu, G., Mennerick, S., and Holtzman, D.M. (2008). Endocytosis Is Required for Synaptic Activity-Dependent Release of Amyloid-beta In Vivo. Neuron *58*, 42-51.
Cossec, J.-C., Simon, A., Marquer, C., Moldrich, R.X., Leterrier, C., Rossier, J., Duyckaerts, C., Lenkei, Z., and Potier, M.-C. (2010). Clathrin-dependent APP endocytosis and Aβ secretion are highly sensitive to the level of plasma membrane cholesterol. Biochimica et Biophysica Acta (BBA) - Molecular and Cell Biology of Lipids *1801*, 846-852.
Darbon, J., Cunha, A., Chan, T.F., Osher, S., and Jensen, G.J. (2008). Fast nonlocal filtering applied to electron cryomicroscopy. Paper presented at: 2008 5th IEEE International Symposium on Biomedical Imaging: From Nano to Macro.
Das, U., Scott, David A., Ganguly, A., Koo, Edward H., Tang, Y., and Roy, S. (2013). Activity-Induced Convergence of APP and BACE-1 in Acidic Microdomains via an Endocytosis-Dependent Pathway. Neuron *79*, 447-460.
Das, U., Wang, L., Ganguly, A., Saikia, J.M., Wagner, S.L., Koo, E.H., and Roy, S. (2015). Visualizing APP and BACE-1 approximation in neurons yields insight into the amyloidogenic pathway. Nature Neuroscience *19*, 55-64.
Dason, J.S., Smith, A.J., Marin, L., and Charlton, M.P. (2010). Vesicular Sterols Are Essential for Synaptic Vesicle Cycling. The Journal of Neuroscience *30*, 15856-15865.
Dason, J.S., Smith, A.J., Marin, L., and Charlton, M.P. (2014). Cholesterol and F-actin are required for clustering of recycling synaptic vesicle proteins in the presynaptic plasma membrane. The Journal of Physiology *592*, 621-633.
De Strooper, B., and Karran, E. (2016). The Cellular Phase of Alzheimer's Disease. Cell *164*, 603-615.
Dzyubenko, E., Rozenberg, A., Hermann, D.M., and Faissner, A. (2016). Colocalization of synapse marker proteins evaluated by STED-microscopy reveals patterns of neuronal synapse distribution in vitro. Journal of neuroscience methods *273*, 149-159.
Ebinu, J.O., and Yankner, B.A. (2002). A RIP Tide in Neuronal Signal Transduction. Neuron *34*, 499-502.
Egawa, J., Pearn, M.L., Lemkuil, B.P., Patel, P.M., and Head, B.P. (2016). Membrane lipid rafts and neurobiology: age-related changes in membrane lipids and loss of neuronal function. The Journal of Physiology *594*, 4565-4579.
Eggert, S., Gonzalez, A.C., Thomas, C., Schilling, S., Schwarz, S.M., Tischer, C., Adam, V., Strecker, P., Schmidt, V., Willnow, T.E*., et al.* (2017a). Dimerization leads to changes in APP (amyloid precursor protein) trafficking mediated by LRP1 and SorLA. Cellular and Molecular Life Sciences.
Eggert, S., Thomas, C., Kins, S., and Hermey, G. (2017b). Trafficking in Alzheimer's Disease: Modulation of APP Transport and Processing by the Transmembrane Proteins LRP1, SorLA, SorCS1c, Sortilin, and Calsyntenin. Molecular Neurobiology.
Fanutza, T., Del Prete, D., Ford, M.J., Castillo, P.E., and D'Adamio, L. (2015). APP and APLP2 interact with the synaptic release machinery and facilitate transmitter release at hippocampal synapses. eLife *4*.

Gamba, P., Testa, G., Sottero, B., Gargiulo, S., Poli, G., and Leonarduzzi, G. (2012). The link between altered cholesterol metabolism and Alzheimer's disease. Annals of the New York Academy of Sciences *1259*, 54-64.
Gibson, D.G., Young, L., Chuang, R.-Y., Venter, J.C., Hutchison, C.A., and Smith, H.O. (2009). Enzymatic assembly of DNA molecules up to several hundred kilobases. Nature Methods *6*, 343-345.
Grimm, M.O.W., Grimm, H.S., Tomic, I., Beyreuther, K., Hartmann, T., and Bergmann, C. (2008). Independent Inhibition of Alzheimer Disease beta- and gamma-Secretase Cleavage by Lowered Cholesterol Levels. Journal of Biological Chemistry *283*, 11302-11311.
Groemer, T.W., Thiel, C.S., Holt, M., Riedel, D., Hua, Y., Huve, J., Wilhelm, B.G., and Klingauf, J. (2011). Amyloid precursor protein is trafficked and secreted via synaptic vesicles. PLoS One *6*, e18754.
Haass, C., Kaether, C., Thinakaran, G., and Sisodia, S. (2012). Trafficking and Proteolytic Processing of APP. Cold Spring Harb Perspect Med *2*, a006270.
Haass, C., Koo, E.H., Mellon, A., Hung, A.Y., and Selkoe, D.J. (1992). Targeting of cell-surface beta-amyloid precursor protein to lysosomes: alternative processing into amyloid-bearing fragments. Nature *357*, 500-503.
Hardy, J., and Allsop, D. (1991). Amyloid deposition as the central event in the aetiology of Alzheimer's disease. Trends in Pharmacological Sciences *12*, 383-388.
Harris, B., Pereira, I., and Parkin, E. (2009). Targeting ADAM10 to lipid rafts in neuroblastoma SH-SY5Y cells impairs amyloidogenic processing of the amyloid precursor protein. Brain Research *1296*, 203-215.
Herr, U.-M., Strecker, P., Storck, S.E., Thomas, C., Rabiej, V., Junker, A., Schilling, S., Schmidt, N., Dowds, C.M., Eggert, S.*, et al.* (2017). LRP1 Modulates APP Intraneuronal Transport and Processing in Its Monomeric and Dimeric State. Frontiers in Molecular Neuroscience *10*.
Huang, Y.-W.A., Zhou, B., Wernig, M., and Südhof, T.C. (2017). ApoE2, ApoE3, and ApoE4 Differentially Stimulate APP Transcription and Aβ Secretion. Cell.
Jiang, M., and Chen, G. (2006). High Ca2+-phosphate transfection efficiency in low-density neuronal cultures. Nature protocols *1*, 695.
Kamal, A., Almenar-Queralt, A., LeBlanc, J.F., Roberts, E.A., and Goldstein, L.S.B. (2001). Kinesin-mediated axonal transport of a membrane compartment containing beta-secretase and presenilin-1 requires APP. Nature *414*, 643-648.
Kang, J., Lemaire, H.G., Unterbeck, A., Salbaum, J.M., Masters, C.L., Grzeschik, K.H., Multhaup, G., Beyreuther, K., and Muller-Hill, B. (1987). The precursor of Alzheimer's disease amyloid A4 protein resembles a cell-surface receptor. Nature *325*, 733-736.
Kim, Y., Kim, C., Jang, H.Y., Mook-Jung, I., and Kim, B. (2016). Inhibition of Cholesterol Biosynthesis Reduces gamma-Secretase Activity and Amyloid-beta Generation. Journal of Alzheimer's Disease *51*, 1057-1068.
Kojro, E., Gimpl, G., Lammich, S., Marz, W., and Fahrenholz, F. (2001). Low cholesterol stimulates the nonamyloidogenic pathway by its effect on the alpha -secretase ADAM 10. Proc Natl Acad Sci U S A *98*, 5815-5820.
Korade, Z., and Kenworthy, A.K. (2008). Lipid rafts, cholesterol, and the brain. Neuropharmacology *55*, 1265-1273.

Kuentzel, S.L., Ali, S.M., Altman, R.A., Greenberg, B.D., and Raub, T.J. (1993). The Alzheimer beta-amyloid protein precursor/protease nexin-II is cleaved by secretase in a trans-Golgi secretory compartment in human neuroglioma cells. Biochemical Journal *295*, 367-378.
Kügler, S., Meyn, L., Holzmüller, H., Gerhardt, E., Isenmann, S., Schulz, J.B., and Bähr, M. (2001). Neuron-Specific Expression of Therapeutic Proteins: Evaluation of Different Cellular Promoters in Recombinant Adenoviral Vectors. Molecular and Cellular Neuroscience *17*, 78-96.
Laßek, M., Weingarten, J., Einsfelder, U., Brendel, P., Müller, U., and Volknandt, W. (2013). Amyloid precursor proteins are constituents of the presynaptic active zone. J Neurochem *127*, 48-56.
Lazarenko, R.M., DelBove, C.E., Strothman, C.E., and Zhang, Q. (2017). Ammonium chloride alters neuronal excitability and synaptic vesicle release. Scientific Reports *7*, 5061.
Li, Y., and Tsien, R. (2012). pHTomato, a red, genetically encoded indicator that enables multiplex interrogation of synaptic activity. Nature Neuroscience *15*, 1047-1053.
Liu, G., and Tsien, R.W. (1995). Synaptic transmission at single visualized hippocampal boutons. Neuropharmacology *34*, 1407-1421.
Liu, Q., Zerbinatti, C.V., Zhang, J., Hoe, H.S., Wang, B., Cole, S.L., Herz, J., Muglia, L., and Bu, G. (2007). Amyloid precursor protein regulates brain apolipoprotein E and cholesterol metabolism through lipoprotein receptor LRP1. Neuron *56*, 66-78.
Liu, W.W., Todd, S., Coulson, D.T.R., Irvine, G.B., Passmore, A.P., McGuinness, B., McConville, M., Craig, D., and Johnston, J.A. (2009). A novel reciprocal and biphasic relationship between membrane cholesterol and beta-secretase activity in SH-SY5Y cells and in human platelets. Journal of Neurochemistry *108*, 341-349.
Mahley, R.W. (2016). Central Nervous System Lipoproteins: ApoE and Regulation of Cholesterol Metabolism. Arterioscler Thromb Vasc Biol *36*, 1305-1315.
Miesenbock, G., De Angelis, D.A., and Rothman, J.E. (1998). Visualizing secretion and synaptic transmission with pH-sensitive green fluorescent proteins. Nature *394*, 192-195.
Muller, U.C., and Zheng, H. (2012). Physiological functions of APP family proteins. Cold Spring Harb Perspect Med *2*, a006288.
Nhan, H.S., Chiang, K., and Koo, E.H. (2015). The multifaceted nature of amyloid precursor protein and its proteolytic fragments: friends and foes. Acta Neuropathol *129*, 1-19.
O'Brien, R.J., and Wong, P.C. (2011). Amyloid Precursor Protein Processing and Alzheimer's Disease. In Annual Review of Neuroscience, Vol 34, S.E. Hyman, T.M. Jessell, C.J. Shatz, C.F. Stevens, and H.Y. Zoghbi, eds., pp. 185-204.
Osborn, M.J., Panoskaltsis-Mortari, A., McElmurry, R.T., Bell, S.K., Vignali, D.A.A., Ryan, M.D., Wilber, A.C., McIvor, R.S., Tolar, J., and Blazar, B.R. (2005). A picornaviral 2A-like sequence-based tricistronic vector allowing for high-level therapeutic gene expression coupled to a dual-reporter system. Molecular Therapy *12*, 569-574.
Parvathy, S., Hussain, I., Karran, E.H., Turner, A.J., and Hooper, N.M. (1999). Cleavage of Alzheimer's Amyloid Precursor Protein by alpha-Secretase Occurs at the Surface of Neuronal Cells. Biochemistry *38*, 9728-9734.
Pfisterer, U., Kirkeby, A., Torper, O., Wood, J., Nelander, J., Dufour, A., Bjorklund, A., Lindvall, O., Jakobsson, J., and Parmar, M. (2011). Direct conversion of human fibroblasts to dopaminergic neurons. Proc Natl Acad Sci U S A *108*, 10343-10348.

Pfrieger, F.W. (2003). Outsourcing in the brain: do neurons depend on cholesterol delivery by astrocytes? Bioessays *25*, 72-78.
Pierrot, N., Tyteca, D., D'Auria, L., Dewachter, I., Gailly, P., Hendrickx, A., Tasiaux, B., Haylani, L.E., Muls, N., N'Kuli, F.*, et al.* (2013). Amyloid precursor protein controls cholesterol turnover needed for neuronal activity. EMBO Molecular Medicine *5*, 608-625.
Pietrzik, C.U., Busse, T., Merriam, D.E., Weggen, S., and Koo, E.H. (2002). The cytoplasmic domain of the LDL receptor-related protein regulates multiple steps in APP processing. The EMBO Journal *21*, 5691-5700.
Pietrzik, C.U., Yoon, I.S., Jaeger, S., Busse, T., Weggen, S., and Koo, E.H. (2004). FE65 constitutes the functional link between the low-density lipoprotein receptor-related protein and the amyloid precursor protein. Journal of Neuroscience *24*, 4259-4265.
Priller, C., Bauer, T., Mitteregger, G., Krebs, B., Kretzschmar, H.A., and Herms, J. (2006). Synapse formation and function is modulated by the amyloid precursor protein. J Neurosci *26*, 7212-7221.
Refolo, L.M., Sambamurti, K., Efthimiopoulos, S., Pappolla, M.A., and Robakis, N.K. (1995). Evidence that secretase cleavage of cell surface Alzheimer amyloid precursor occurs after normal endocytic internalization. Journal of Neuroscience Research *40*, 694-706.
Reinhard, C., Hebert, S.S., and De Strooper, B. (2005). The amyloid-beta precursor protein: integrating structure with biological function. EMBO J *24*, 3996-4006.
Rohan de Silva, H.A., Jen, A., Wickenden, C., Jen, L.S., Wilkinson, S.L., and Patel, A.J. (1997). Cell-specific expression of beta-amyloid precursor protein isoform mRNAs and proteins in neurons and astrocytes. Brain Res Mol Brain Res *47*, 147-156.
Runz, H., Rietdorf, J., Tomic, I., de Bernard, M., Beyreuther, K., Pepperkok, R., and Hartmann, T. (2002). Inhibition of intracellular cholesterol transport alters presenilin localization and amyloid precursor protein processing in neuronal cells. J Neurosci *22*, 1679-1689.
Schindelin, J., Arganda-Carreras, I., Frise, E., Kaynig, V., Longair, M., Pietzsch, T., Preibisch, S., Rueden, C., Saalfeld, S., Schmid, B.*, et al.* (2012). Fiji: an open-source platform for biological-image analysis. Nature Methods *9*, 676-682.
Schneider, A., Rajendran, L., Honsho, M., Gralle, M., Donnert, G., Wouters, F., Hell, S.W., and Simons, M. (2008). Flotillin-Dependent Clustering of the Amyloid Precursor Protein Regulates Its Endocytosis and Amyloidogenic Processing in Neurons. The Journal of Neuroscience *28*, 2874-2882.
Schneider, C.A., Rasband, W.S., and Eliceiri, K.W. (2012). NIH Image to ImageJ: 25 years of image analysis. Nature Methods *9*, 671-675.
Sebastião, A.M., Colino-Oliveira, M., Assaife-Lopes, N., Dias, R.B., and Ribeiro, J.A. (2013). Lipid rafts, synaptic transmission and plasticity: Impact in age-related neurodegenerative diseases. Neuropharmacology *64*, 97-107.
Selkoe, D.J., and Hardy, J. (2016). The amyloid hypothesis of Alzheimer's disease at 25 years. EMBO Mol Med *8*, 595-608.
Shinohara, M., Tachibana, M., Kanekiyo, T., and Bu, G.J. (2017). Thematic Review Series: ApoE and Lipid Homeostasis in Alzheimer's Disease Role of LRP1 in the pathogenesis of Alzheimer's disease: evidence from clinical and preclinical studies. Journal of Lipid Research *58*, 1267-1281.
Simons, K., and Gerl, M.J. (2010). Revitalizing membrane rafts: new tools and insights. Nature Reviews Molecular Cell Biology *11*, 688.

Song, Y., Hustedt, E.J., Brandon, S., and Sanders, C.R. (2013). Competition between homodimerization and cholesterol binding to the C99 domain of the amyloid precursor protein. Biochemistry *52*, 5051-5064.
Sun, J., and Roy, S. (2017). The physical approximation of APP and BACE-1 - a key event in Alzheimer's disease pathogenesis. Developmental Neurobiology.
Takamori, S., Holt, M., Stenius, K., Lemke, E.A., Gronborg, M., Riedel, D., Urlaub, H., Schenck, S., Brugger, B., Ringler, P.*, et al.* (2006). Molecular anatomy of a trafficking organelle. Cell *127*, 831-846.
Tamboli, I.Y., Prager, K., Thal, D.R., Thelen, K.M., Dewachter, I., Pietrzik, C.U., St. George-Hyslop, P., Sisodia, S.S., De Strooper, B., Heneka, M.T.*, et al.* (2008). Loss of gamma-Secretase Function Impairs Endocytosis of Lipoprotein Particles and Membrane Cholesterol Homeostasis. Journal of Neuroscience *28*, 12097-12106.
Thevenaz, P., Ruttimann, U.E., and Unser, M. (1998). A pyramid approach to subpixel registration based on intensity. IEEE Transactions on Image Processing *7*, 27-41.
Toh, W.H., and Gleeson, P.A. (2016). Dysregulation of intracellular trafficking and endosomal sorting in Alzheimer's disease: controversies and unanswered questions. Biochemical Journal *473*, 1977-1993.
Ulery, P.G., Beers, J., Mikhailenko, I., Tanzi, R.E., Rebeck, G.W., Hyman, B.T., and Strickland, D.K. (2000). Modulation of beta-amyloid precursor protein processing by the low density lipoprotein receptor-related protein (LRP) - Evidence that LRP contributes to the pathogenesis of Alzheimer's disease. Journal of Biological Chemistry *275*, 7410-7415.
Villegas, C., Muresan, V., and Ladescu Muresan, Z. (2014). Dual-tagged amyloid-beta precursor protein reveals distinct transport pathways of its N- and C-terminal fragments. Hum Mol Genet *23*, 1631-1643.
von Arnim, C.A., von Einem, B., Weber, P., Wagner, M., Schwanzar, D., Spoelgen, R., Strauss, W.L., and Schneckenburger, H. (2008). Impact of cholesterol level upon APP and BACE proximity and APP cleavage. Biochem Biophys Res Commun *370*, 207-212.
Wagner, T., and Pietrzik, C.U. (2012). The role of lipoprotein receptors on the physiological function of APP. Experimental Brain Research *217*, 377-387.
Wang, H., Megill, A., He, K., Kirkwood, A., and Lee, H.-K. (2012). Consequences of Inhibiting Amyloid Precursor Protein Processing Enzymes on Synaptic Function and Plasticity. Neural Plasticity *2012*, 1-24.
Wang, Z., Jackson, R.J., Hong, W., Taylor, W.M., Corbett, G.T., Moreno, A., Liu, W., Li, S., Frosch, M.P., Slutsky, I.*, et al.* (2017). Human brain-derived Abeta oligomers bind to synapses and disrupt synaptic activity in a manner that requires APP. J Neurosci.
Wei, W., Nguyen, L.N., Kessels, H.W., Hagiwara, H., Sisodia, S., and Malinow, R. (2010). Amyloid beta from axons and dendrites reduces local spine number and plasticity. Nat Neurosci *13*, 190-196.
Wilhelm, B.G., Mandad, S., Truckenbrodt, S., Krohnert, K., Schafer, C., Rammner, B., Koo, S.J., Classen, G.A., Krauss, M., Haucke, V.*, et al.* (2014). Composition of isolated synaptic boutons reveals the amounts of vesicle trafficking proteins. Science *344*, 1023-1028.
Willem, M., Tahirovic, S., Busche, M.A., Ovsepian, S.V., Chafai, M., Kootar, S., Hornburg, D., Evans, L.D.B., Moore, S., Daria, A.*, et al.* (2015). η-Secretase processing of APP inhibits neuronal activity in the hippocampus. Nature *526*, 443-447.

Wood, W.G., Igbavboa, U., Muller, W.E., and Eckert, G.P. (2011). Cholesterol asymmetry in synaptic plasma membranes. J Neurochem *116*, 684-689.
Wood, W.G., Schroeder, F., Igbavboa, U., Avdulov, N.A., and Chochina, S.V. (2002). Brain membrane cholesterol domains, aging and amyloid beta-peptides. Neurobiology of Aging *23*, 685-694.
Xiong, H., Callaghan, D., Jones, A., Walker, D.G., Lue, L.-F., Beach, T.G., Sue, L.I., Woulfe, J., Xu, H., Stanimirovic, D.B.*, et al.* (2008). Cholesterol retention in Alzheimer's brain is responsible for high beta- and gamma-secretase activities and Aβ production. Neurobiology of Disease *29*, 422-437.
Yan, Y., Xu, T.-H., Harikumar, K.G., Miller, L.J., Melcher, K., and Xu, H.E. (2017). Dimerization of the transmembrane domain of amyloid precursor protein is determined by residues around the gamma-secretase cleavage sites. Journal of Biological Chemistry.
Yue, H.-Y., and Xu, J. (2015). Cholesterol regulates multiple forms of vesicle endocytosis at a mammalian central synapse. Journal of Neurochemistry *134*, 247-260.
Zhang, Q., Li, Y., and Tsien, R.W. (2009). The dynamic control of kiss-and-run and vesicular reuse probed with single nanoparticles. Science *323*, 1448-1453.

Figure Legends

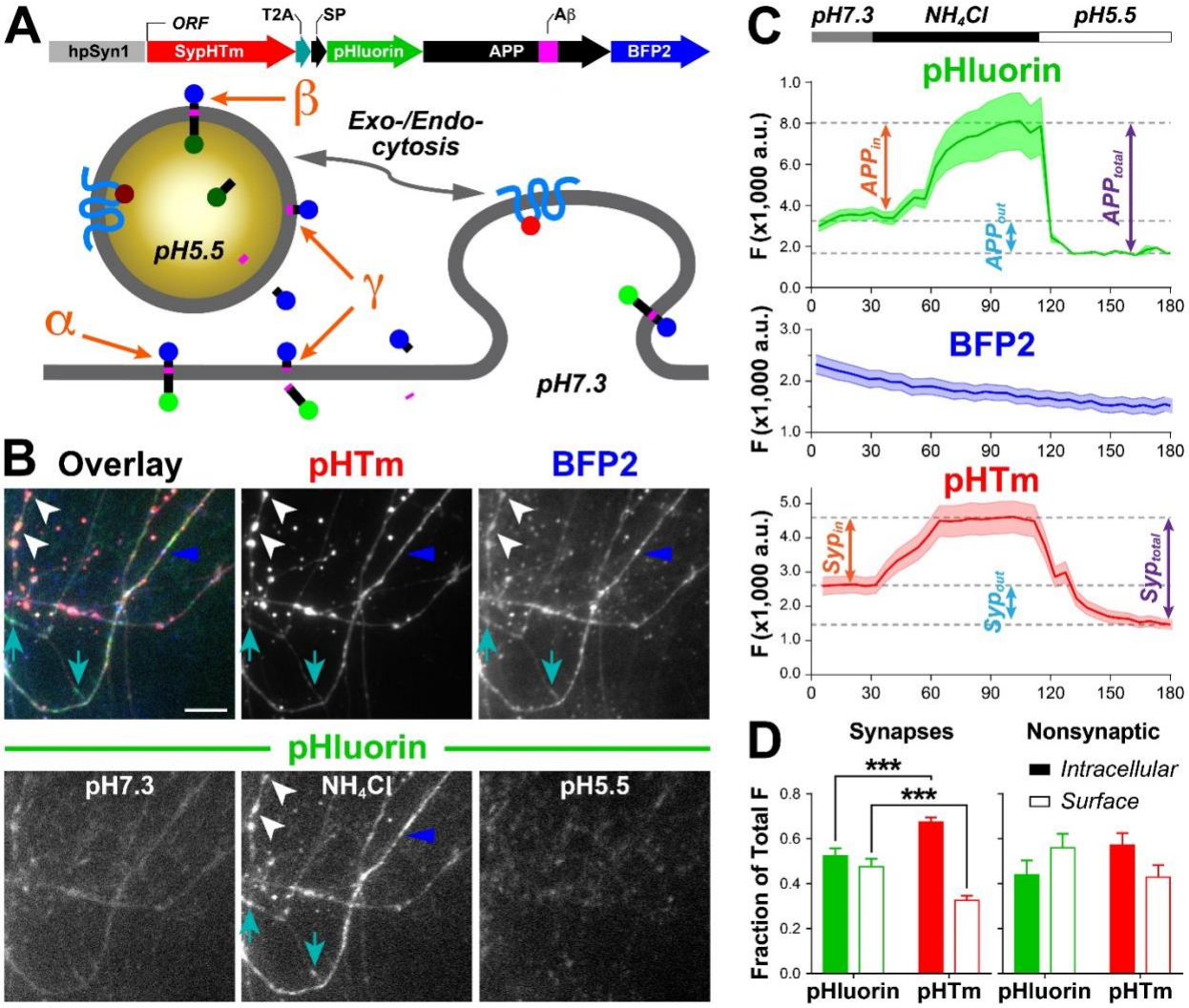

Figure 1. SypHTm:T2A:pH-APP-BFP2 reports APP distribution and marks synaptic vesicles. A, top diagram illustrates the components of SypHTm:T2A:pH-APP-BFP2 including the human Synapsin I promoter (hpSyn1) and an open reading frame (ORF) comprised of Synaptophysin-pHTomato (SypHTm), *thosea asigna* virus 2A peptide (T2A), APP signal peptide (SP), pH-sensitive green fluorescent protein (pHluorin), APP containing Aβ, and blue fluorescence protein 2 (BFP2). The lower cartoon demonstrates how extracellular pH and exo-/endocytosis affect pHluorin and pHTm fluorescence and how α-, β-, and γ-secretases cleave pH-APP-BFP2. **B**, top left, overlay of SypHTm (red),

pHluorin (green) in 50 mM NH_4Cl, and BFP2 (blue); top middle, SypHTom in 50 mM NH_4Cl; top right, averaged BFP2 throughout the course of the experiment; bottom: pHluorin in normal Tyrode's solution (pH7.3), in 50 mM NH_4Cl and in pH5.5 Tyrode's solution. White arrowheads indicate synaptically co-localized SypHTm and pH-APP-BFP2, cyan arrows indicate non-synaptic pH-APP-BFP2, and the blue arrowheads indicate nonsynaptic CTF because of strong BFP2 and weak pHluorin signals. Scale bar, 10 µm. **C**, example of intensity changes of pHluorin, BFP2 and pHTm fluorescence in one FOV (field of view) containing 39 ROIs (regions of interest) during sequential applications of pH7.3 Tyrode's solution, 50 mM NH_4Cl and pH5.5 Tyrode's solution. Double-ended arrows indicate the calculations of surface, intracellular and total APP and Syp based on fluorescence intensity differences. Shades are s.e.m. **D**, quantification of intracellular (solid bars) and surface (open bars) pHluorin (green) and pHTm (red) fluorescence at synapses (left) and nonsynaptic areas (right). There was a significant difference between pHTm and pHluorin regarding surface or intracellular fractions according to a two-tailed paired *t* test (***, $p = 0.001$). No significant difference was found for the nonsynaptic ROIs (two-tailed paired t-test, ns, $p = 0.0543$). Synaptic ROIs, n = 47; nonsynaptic ROIs, n = 23. All error bars represent s.e.m.

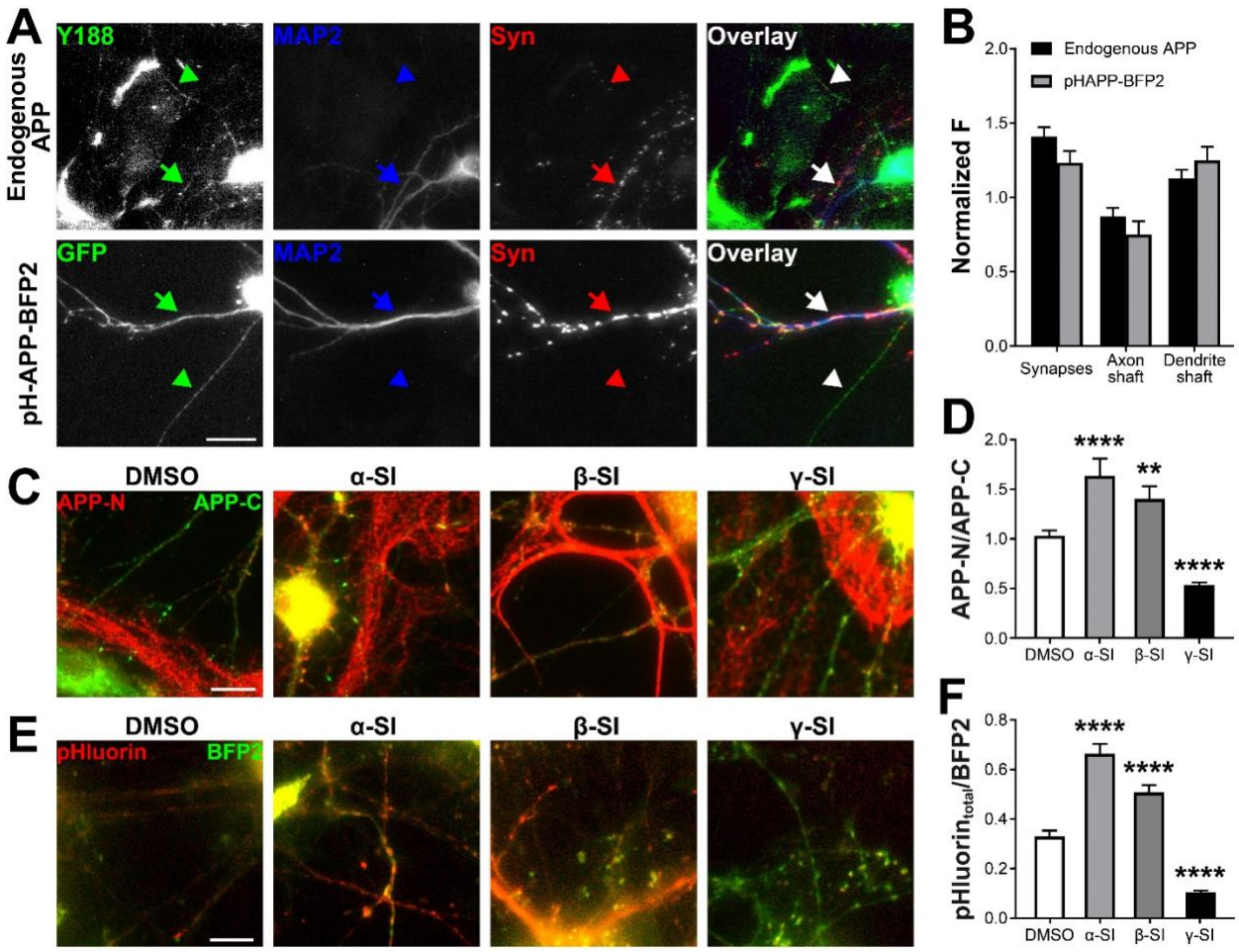

Figure 2. pH-APP-BFP2 is distributed and cleaved in the same way as endogenous APP is. A, sample images of immunofluorescence labeling of untransfected (top) and transfected cells (bottom). The Y188 antibody was used to detect endogenous APP (green), and anti-GFP antibody was used to detect transgenically expressed pH-APP-BFP2 (green). Anti-MAP2 antibody was used to identify dendrites (arrows) and thin neurites with low expression of MAP2 (arrowheads). Anti-Syn was used to identify synaptic boutons. Scale bar, 100 μm. **B**, normalized average APP fluorescence in synaptic boutons, axon shafts and dendritic shafts, normalized to the average fluorescence of the whole processes. Two-way ANOVA detected a significant effect of localization at synapses, axonal shafts and dendritic shafts ($F(2, 30) = 25.29$, $p < 0.0001$).

There was no significant difference between pH-APP-BFP2 and endogenous APP (F (1, 30) = 0.9346, p = 0.3414) and no interaction between the two factors (F (2, 30) = 2.256, p = 0.1223). **C**, sample images of immunofluorescence labeling for APP N- and C-terminals with and without secretase inhibitors (α/β/γ-SI). Scale bar, 50 μm. **D**, one-way ANOVA detected significant differences in the endogenous APP N/C ratio after α/β/γ-SI treatments (F (3, 380) = 44.153, p < 0.0001). Dunnett's multiple comparisons test showed that α/βSI increased the ratio compared to DMSO (****, p = 0.0001; and **, p = 0.0014, respectively). γSI significantly decreased the ratio (****, p = 0.0001). DMSO, n = 160; α-SI, n = 21; β-SI, n = 38; γ-SI, n = 165, where n is the number of Syp-positive puncta (i.e. synaptic boutons). **E**, sample images of live cell imaging for total pHluorin (for APP's N-terminal, red color) and total BFP2 (for APP's C-terminal, green color) after α/β/γ-SI treatments. Scale bar, 10 μm. **F**, pHluorin/BFP2 ratio after SI treatments. One-way ANOVA detected a significant effect (F (3, 499) = 98.199, p < 0.0001) and Dunnett's multiple comparisons test showed that α-SI and β-SI both increased the ratio compared to DMSO (****, p = 0.0001; ****, p = 0.0001) while γ-SI decreased it (****, p = 0.0001). DMSO, n = 132; α-SI, n = 126; β-SI, n = 80; γ-SI, n = 165, where n is the number of ROIs corresponding to Syp-marked synaptic boutons. All error bars represent s.e.m.

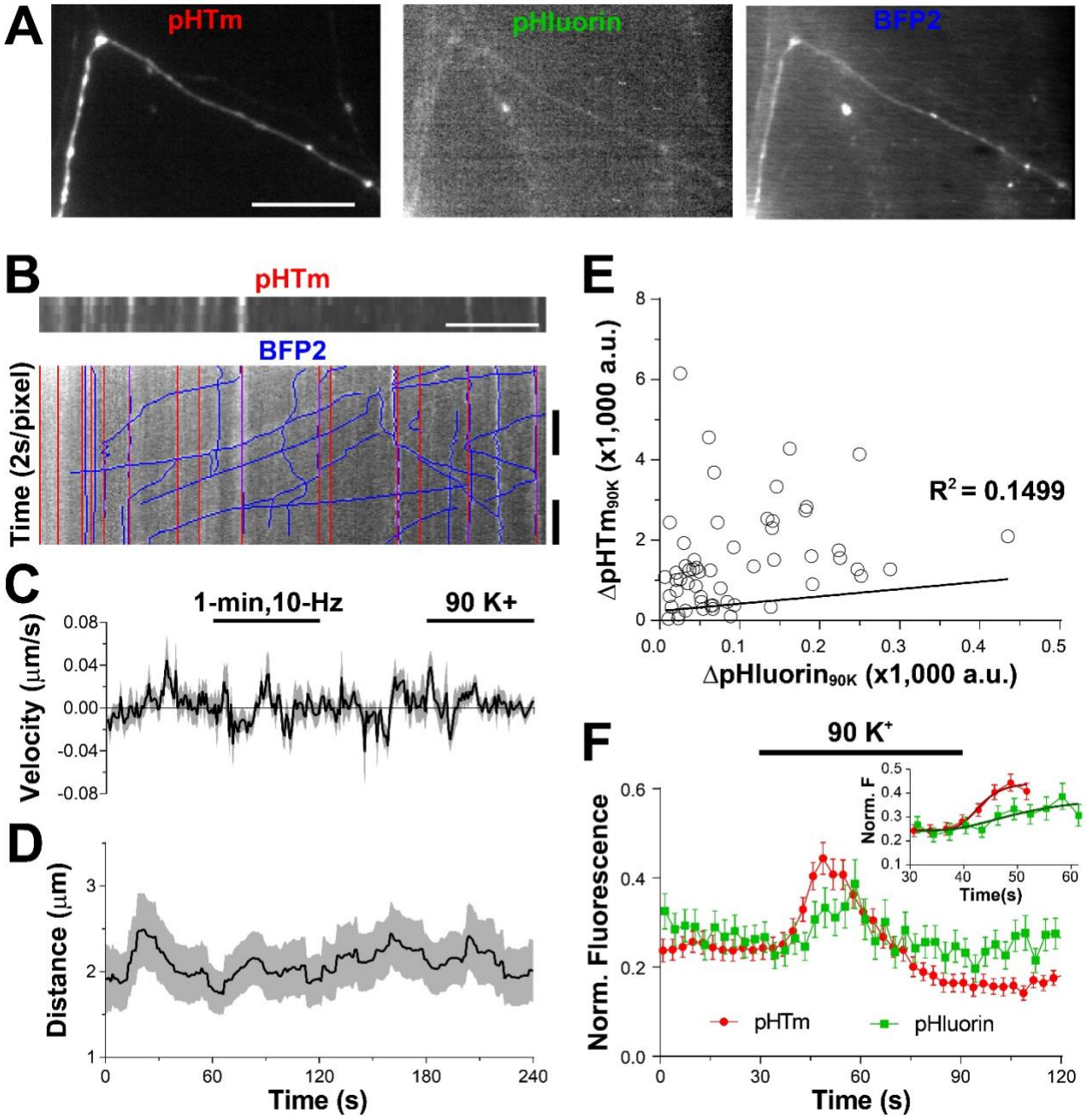

Figure 3. APP trafficking is not activity-associated.

A, sample images of a process in 3 fluorescence channels. Scale bar, 10 µm. **B**, sample kymographs that show the changes in value over time during 10 Hz field stimulation and 90K stimulation along the process shown in **A**. BFP2 was imaged every two seconds, while pHTm was imaged every minute for relatively immobile synaptic boutons. Hand

drawn BFP2 tracks are shown in blue, immobile synaptic boutons are in red, and purple is overlap. **C**, mean velocity of the moving BFP2 puncta. Movement towards the nearest synapse was defined as positive. **D**, mean distance from the moving BFP2 puncta to the nearest synapse. For **C-D**, only visible puncta contribute to the mean and s.e.m, with at most 81 puncta and at least 50 puncta at any given time. There was a total of 241 tracks taken from 13 kymographs from 4 experiments. **E,** $pHTm_{90K}$ and $pHluorin_{90K}$ represent the maximal increase of fluorescence during 90 mM K^+ perfusion. n = 56 ROIs from 3 experiments. The line shows a linear regression of slope 1.25 ± 0.36. There is a small but significant correlation: Pearson's R^2 = 0.1499, p = 0.0032. One negative value was excluded. **F**, synaptic pHluorin and pHTm fluorescence normalized to the maximal values set by 50 mM NH_4Cl. The pHluorin increase during stimulation with 90 mM K^+ is significantly smaller than that of pHTm according to an unpaired two-tailed *t*-test (p = 0.0224). n = 56 ROIs from 3 FOV. The inset shows variable slope (4 parameters) curves fits to the rising phases of pHTm and pHluorin (30 - 60s) with the constraints Top = 0.4437 or Top = 0.3864, which are the maximums of pHTm and pHluorin, respectively. Based on the fittings, for pHTm, $t_{1/2}$ = 12.98 s; for pHluorin, $t_{1/2}$ = 20.15 s. All shadows (**C, D**) or error bars (**F**) represent s.e.m.

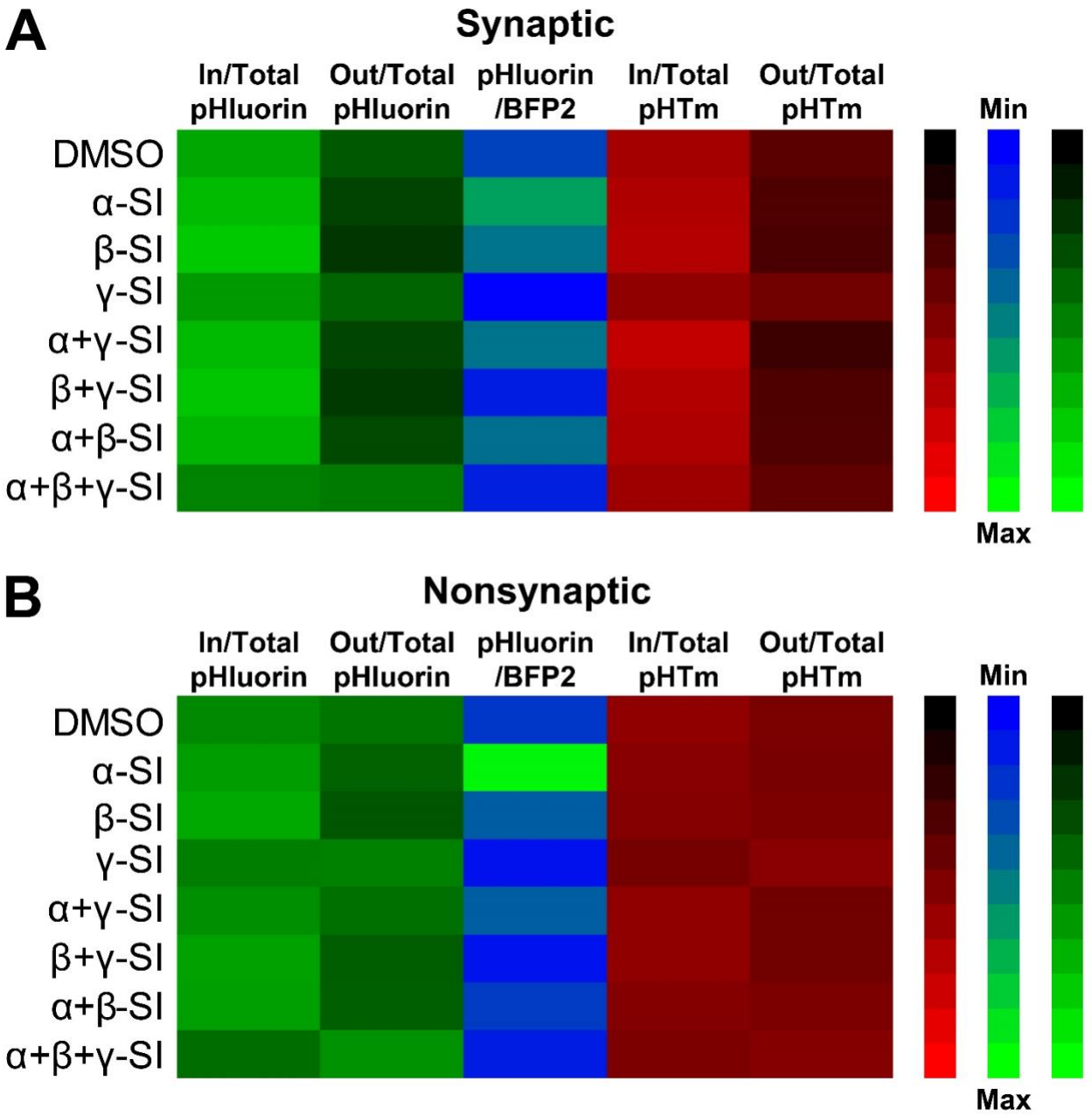

Figure 4. Changes of pHluorin and pHTm ratios after secretase inhibition

A, color-coded representation of the fluorescence ratios at synaptic boutons marked by SypHTm. Color coding and scale are shown in the right. **B**, color-coded representation of the fluorescence ratios at non-synaptic part of the neurites. Color coding and scale are shown in the right. Statistics are shown in **Supplementary Table 2**. Parts of these data sets are also used in **Figure 2E**&**F** and **Supplementary Figure 3**.

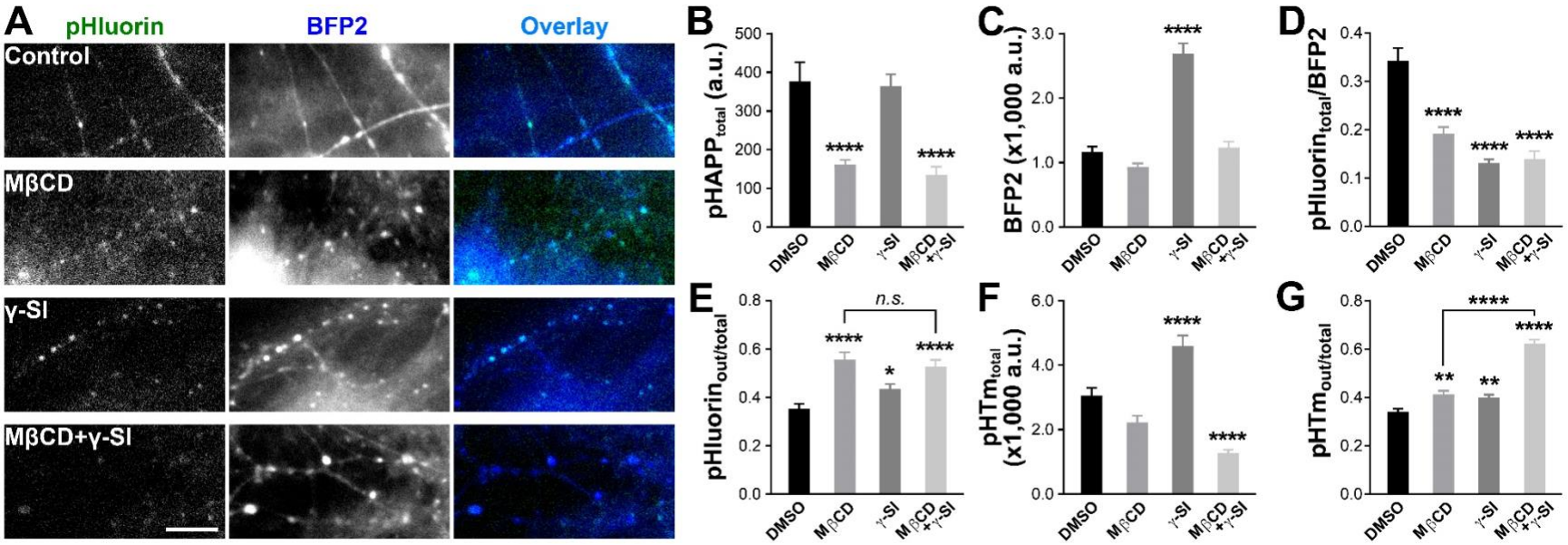

Figure 5. Membrane cholesterol affects the distribution and cleavage of APP.

A, sample images of pHluorin, BFP2 and their overlays with four different treatments. Scale bar, 10 µm. **B**, average total pHluorin fluorescence intensities in synaptic boutons marked by SypHTm. One-way ANOVA detected significant differences among treatments (F (3, 360) = 14.93, $p < 0.0001$). Dunnett's multiple comparisons test showed that MβCD significantly decreased total pHluorin fluorescence without or with γ-SI (****, $p = 0.0001$ for both). However, γ-SI alone made no difference ($p = 0.9834$). **C**, average BFP2 fluorescence intensities in synaptic boutons marked by SypHTm. One-way ANOVA detected significant differences among treatments (F (3, 360) = 48.65, $p < 0.0001$). Dunnett's multiple comparisons test showed that only γ-SI significantly increased BFP2 fluorescence compared to WT (****, $p = 0.0001$). **D**, average total pHluorin vs. BFP2

ratio in synaptic boutons marked by SypHTm. One-way ANOVA detected significant differences among treatments (F (3, 360) = 35.04, $p < 0.0001$). Dunnett's multiple comparisons test showed that MβCD, γ-SI and MβCD+γ-SI significantly decreased the ratio (****, $p = 0.0001$). **E**, average surface vs. total pHluorin ratio in synaptic boutons marked by SypHTm. One-way ANOVA detected significant differences among treatments (F (3, 360) = 12.9832, $p < 0.0001$). Dunnett's multiple comparisons test showed that both MβCD and γ-SI significantly increased the ratio (****, $p = 0.0001$; *, $p = 0.0343$, respectively), as did the combination (****, $p = 0.0001$), but there is no additive effect for MβCD and γ-SI combined compared to MβCD alone (two-tailed unpaired t test, $p = 0.4855$). **F**, average total pHTm in synaptic boutons marked by SypHTm. One-way ANOVA detected significant differences among treatments (F (3, 360) = 30.86, $p < 0.0001$). Dunnett's multiple comparisons test showed that γ-SI significantly increased total pHTm (****, $p = 0.0001$), whereas MβCD and MβCD+γ-SI decreased it (n.s., $p = 0.0888$; ****, $p = 0.0001$, respectively). **G**, average surface vs. total pHTm in synaptic boutons marked by SypHTm. One-way ANOVA detected significant differences among treatments (F (3, 360) = 76.19, $p < 0.0001$). Dunnett's multiple comparisons test showed that MβCD, γ-SI and MβCD+γ-SI significantly increased the ratio (**, $p = 0.0014$; **, $p = 0.003$; ****, $p = 0.0001$, respectively). Additionally, a two-tailed t-test showed a very significant difference between MβCD+γ-SI and MβCD (****, $p < 0.0001$). For **B**-**G**, DMSO, n = 90 (FOV = 5); MβCD, n = 75 (FOV = 5); γ-SI, n = 119 (FOV = 7); MβCD+γ-SI, n = 80 ROIs (FOV = 4), where n is the number of ROIs corresponding to SypHTm-marked synaptic boutons.

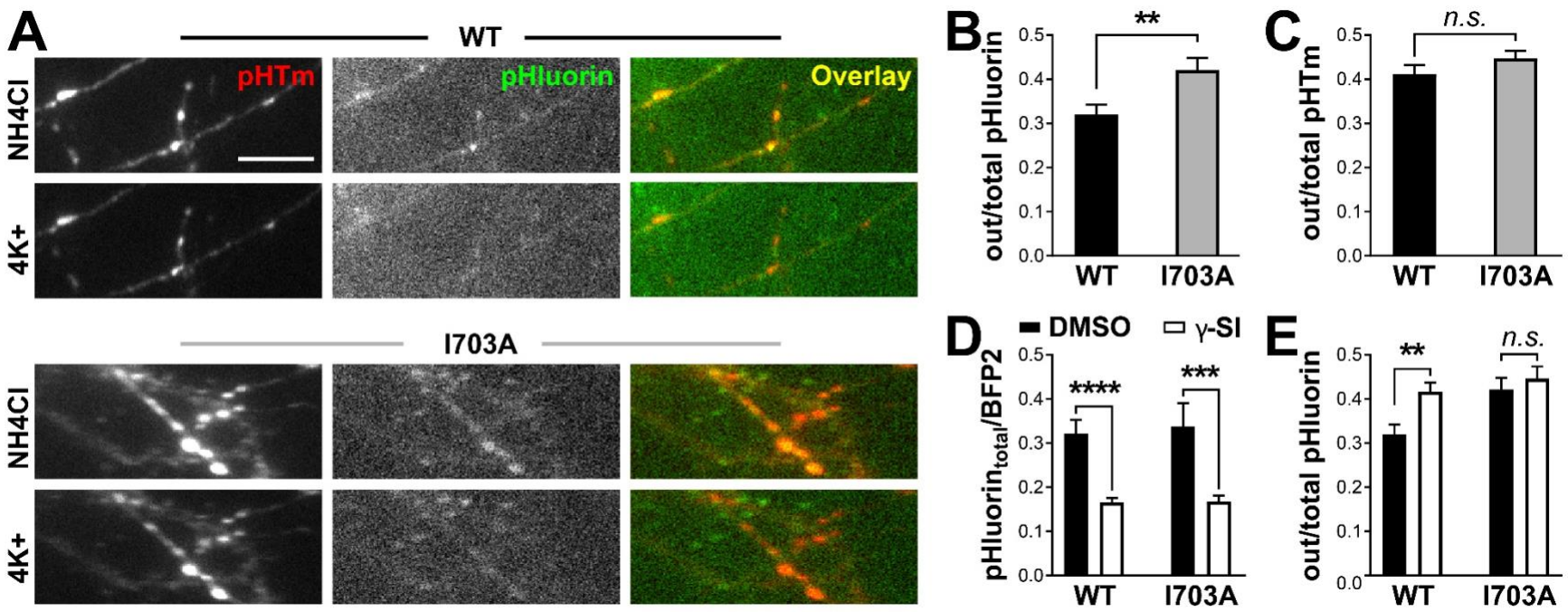

Figure 6. Point mutation within APP's cholesterol-binding motif increases surface APP fraction.

A, sample images of pHTm, pHluorin and their overlays under 50 mM NH_4Cl or $4K^+$ normal Tyrode's solution. Scale bar, 10 µm. **B**, average surface vs. total pHluorin ratio in synaptic boutons marked by SypHTm. An unpaired, two-tailed t test detected significant differences between wildtype and I703A point mutation (**, p = 0.0039). WT, n = 84 (FOV = 6); I703A, n = 68 (FOV = 4), where n is the number of ROIs corresponding to SypHTm-marked synaptic boutons. **C**, average surface vs. total pHTm ratio in synaptic boutons marked by SypHTm. An unpaired, two-tailed t test did not detect a significant difference (p = 0.2345. Same data set as **B**). **D**, average total pHluorin vs. BFP2 ratio in synaptic boutons marked by

SypHTm. Two-way ANOVA detected a significant difference between DMSO and γ-SI (F (1, 323) = 30.86, $p < 0.0001$). Sidak's multiple comparisons test showed that γ-SI significantly decreased the ratio regardless of genotype (WT, ****, $p < 0.0001$; I703A, ***, $p = 0.0004$). There was no difference with respect to genotype (F (1, 323) = 0.1035, $p = 0.7479$) and no interaction between treatment and genotype (F (1, 323) = 0.0497, $p = 0.8237$). For WT and I703A, it is the same data set as **B**; WT+γ-SI, n = 112 (FOV=4); I703A+γ-SI, n = 63 (FOV = 3), where n is the number of ROIs corresponding to SypHTm-marked synaptic boutons**.** **E**, average surfaced vs. total pHluorin ratio in synaptic boutons marked by SypHTm. Two-way ANOVA was used to investigate the effects of γ-inhibition on the mutants. The mutation (F (1, 323) = 7.122, $p = 0.008$) and γ-SI treatment (F (1, 323) = 6.228, $p = 0.0131$) both affect surface fraction, but no interaction was found (F (1, 323) = 2.185, $p = 0.1403$). Sidak's multiple comparisons test was used to compare vehicle control to γ-SI, revealing that γ-SI significantly increased the surface fraction of the wild-type (**, $p = 0.0039$) but not the mutant ($p = 0.7599$). This is based on the same data set as **D**. All error bars are s.e.m.

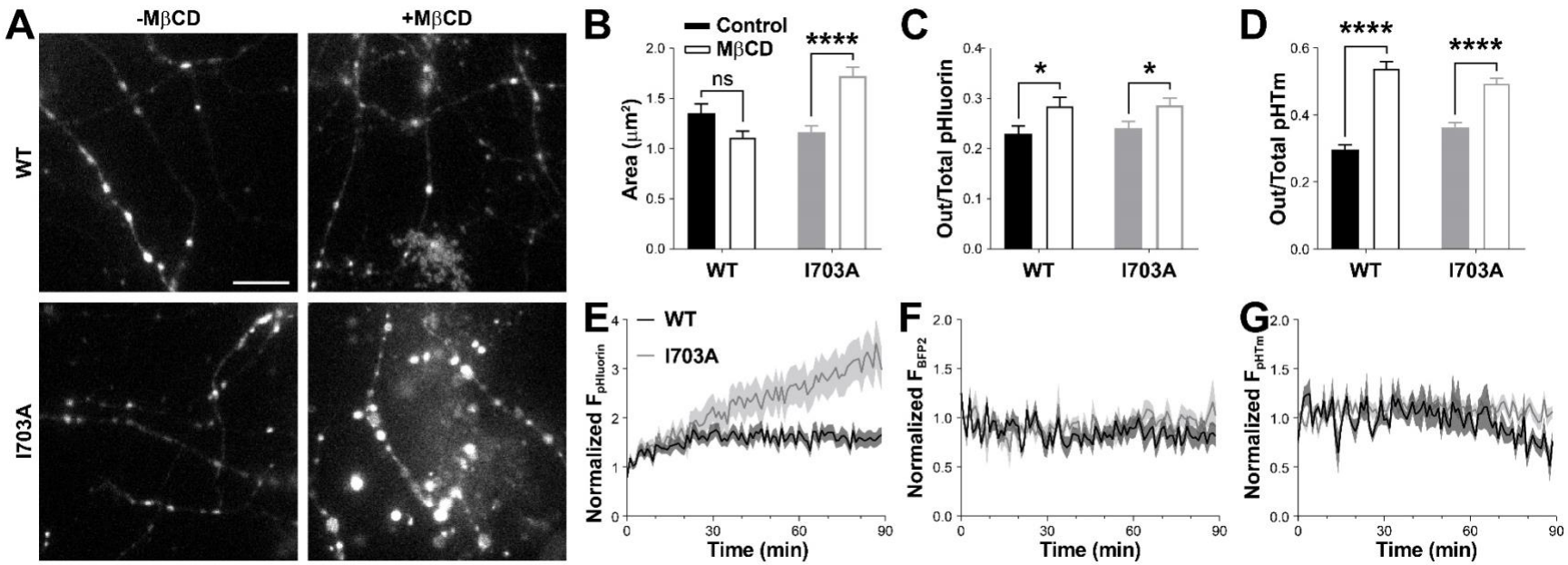

Figure 7. Point mutation in the cholesterol-binding motif renders presynaptic terminals vulnerable to membrane cholesterol reduction.

A, sample pHTm images of cells expressing wild type (WT) and mutant (I703A) pH-APP-BFP2 with or without MβCD treatment. Fields of view were not excluded based on failure to respond to NH_4Cl (provided that they responded to pH 5.5), because dead or otherwise compromised cells and synapses are intended to be included in this analysis. Scale bar, 10 μm. **B,** mean area of synapses. Two-way ANOVA found a significant interaction between the mutation and treatment ($F(1, 746) = 21.34$, $p < 0.0001$), a singificant difference between the WT and I703A ($F(1, 746) = 6.341$, $p = 0.0120$), but treatment itself failed to reach significance ($F(1, 746) = 3.33$, $p = 0.0684$). Sidak's mutliple comparisons test showed, in fact, that the

MβCD's effect on synapse size is specific to I703A (p <0.0001) and does not occur in the WT (p = 0.1589). WT, n = 129 (FOV = 3); WT + MβCD, n = 135 (FOV = 4); I703A, n = 230 (FOV = 3); I703A + MβCD, n = 256 (FOV = 5), where n is the number of ROIs corresponding to SypHTm-marked synaptic boutons. **C**, average surface vs. total pHluorin ratios of two genotypes with or without MβCD treatment. Two-way ANOVA detected a significant difference after MβCD (F (1, 746) = 11.16, *p* = 0.0009). No interaction (F (1, 746) = 0.1938, *p* = 0.7355) and no effect due to the mutation (F (1, 746) = 0.1938, *p* = 0.6599) detected. Sidak's multiple comparisons test showed that MβCD significantly increased the ratio in WT and I703A (*, *p* = 0.0446; *, *p* = 0.0232, respectively. Same data set as **B**). **D**, average surface vs. total pHTm ratios of two genotypes with or without MβCD treatment. Two-way ANOVA detected significant differences between treatments (F (1, 746) = 134.7, *p* < 0.0001) but not genotype (F (1, 746) = 0.5147, *p* = 0.4733), however there was an interaction (F (1, 746) = 11.81, *p* = 0.0006). Sidak's multiple comparisons test showed that MβCD had a significant effect on the ratio for WT and I703A (****, *p* < 0.0001 and ****, *p* < 0.0001. Same data set as **B**). **E-G**, average fluorescence changes of pHluorin. WT, n = 48 ROIs; I703A, n = 53 ROIs. (**E**), BFP2 (**F**) and pHTm (**G**) in WT (black) and I703A mutant (gray) during 90-min 0.5-mM MβCD treatment. Only pHluorin in the mutant group exhibited a consistent increase throughout the treatment. Fluorescence intensities were normalized to pretreatment baseline (set as 1). Shadows represent s.e.m.

Experimental Procedures

DNA recombination

The pHluorin-APP plasmid, which contains a human synapsin1 promoter, was a gift from Dr. Jürgen Klingauf (Groemer et al., 2011). The Synaptophysin-pHTomato plasmid (pTGW-UAS-SypHTm-T2A-BFP2) was a gift from Dr. Yulong Li (Li and Tsien, 2012). The SypHTm fragment was amplified from the Synaptophysin-pHTomato plasmid and inserted into a mammalian expression vector (pCDNA3.1) containing human synapsin1 promoter using Gibson Assembly Cloning Kit (NEB) (Gibson et al., 2009). SypHTm along with the T2A linker was amplified from the pTGW-UAS-SypHTm-2ABFP2 with Phusion kit (NEB) and using 5'-CGTGCCTGAGAGCGCAGTCGAATTAGCTTGGTACCATGGACGTGGTGAATCAGCTGGTGG -3' (forward primer) and 5'-CCAGGCTGGGCAGCATGGTGGCGGCGGATCCAGGGCCGGGATTCTCCTCCACGTCAC-3' (reverse primer). SypHTm:T2A:pH-APP was verified by sequencing. Next, BFP2 was amplified from pTGW-UAS-SypHTm-T2A-BFP2 using 5'-CAAGTTCTTTGAGCAGATGCAGAACGCAGCGGCCGCAATGGTGAGCAAGGGCGAGGAGC -3' (forward primer) and 5'-CATTTAGGTGACACTATAGAATAGGGCCCTCTAGATTACTTGTACAGCTCGTCCATGCCG -3' (reverse primer), and was inserted to the C-terminal of pHluorin-APP before the stop codon using the Gibson Assembly Cloning Kit (NEB). The resulting plasmid, SypHTm:T2A:pH-APP-BFP2 was verified by DNA sequencing.

Cell Culture and Transfection

All animal protocols were approved by the Vanderbilt University Animal Care and Use Committee. Rat postnatal hippocampal cultures were prepared according to an established protocol (Liu and Tsien, 1995) with slight modifications. Briefly, rat hippocampi (CA1-CA3) dissected from P0 or P1 Sprague-Dawley rats were dissociated via an 11-min incubation in Trypsin-EDTA (Life Technologies) followed by gentle trituration using three glass pipettes of different diameters (~1 mm, 0.5 mm, and 0.2 mm), sequentially. Dissociated cells in suspension were recovered by centrifugation (x 200 g, 5 minutes) at 4°C and re-suspended in plating media consisting of Minimal Essential Medium (MEM, Life Technologies) and (in mM) 27 glucose, 2.4 NaHCO3, 0.00125 transferrin, 2 L-glutamine, 0.0043 insulin and 10%/vol fetal bovine serum (FBS, Omega). 100 µl of resuspended cells were plated onto single round 12mm-ø glass coverslip (~200,000 cells/mL) pre-coated with Matrigel (Life Technologies) and all coverslips were placed in 24-well plates (ThermoScientific). Cells were allowed to adhere to the coverslips for 30-60 minutes before the addition of 1 mL plating media per well. After 1-2 days in culture, an additional 1 mL media containing (in mM) 27 glucose, 2.4 $NaHCO_3$, 0.00125 transferrin, 0.5 L-glutamine, 2 Ara-C, 1 %/vol B27 supplement (Life Technologies) and 5 %/vol FBS was added into every well. Ara-C in the culture media efficiently prevented the overgrowth of astroglia. Calcium phosphate transfection was performed at 8-9 days and most experiments were performed at 14-17 days after the full maturation of neuronal synapses.

Immunocytochemistry

After treatments or imaging, coverslips were fixed in PBS containing 4% paraformaldehyde for 20 minutes, permeabilized with 0.25% Triton X-100 for 10 minutes and blocked for at least one hour with goat serum and BSA solution all at room temperature (substituting horse serum if a goat primary was used). Next, they were incubated with diluted primary antibodies (see Supplementary table S1) overnight at 4 ºC or at room temperature for at least one hour. After incubation with primary antibodies, cells were thoroughly washed and then incubated with specific secondary antibodies labeled by distinct fluorophores (see **Supplementary Table S1**, 1: 1000 dilution for all, Life Technologies or Biotium) at room temperature for at least one hour before mounting.

Filipin and AM1-43 dual staining

Coverslips were removed from their incubator and washed briefly in pre-warmed (37°C) 4K Tyrode. AM1-43 was diluted in 90K solution and applied to the cells for 1 minute at room temperature. After at least 2 gentle washes with room temperature PBS, the cells were fixed for 30 minutes in 4% paraformaldehyde. The paraformaldehyde was quenched with 1.5 mg/mL glycine in PBS for 10 minutes at room temperature before washing in PBS. Filipin solution (0.05 mg/mL in PBS) was applied to the cells. In order to minimize Filipin permeabilization of the cells, the staining was performed at 4°C for 30 minutes only. The coverslips were then washed and mounted.

ELISA

The Mouse/Rat sAPPα (highly sensitive) Assay Kit (IBL #27419) was used to measure the sAPPα concentration in the undiluted media. Serum-containing culture media was

removed and replaced with 1mL of serum-free NeuroBasal media supplemented with 2 mM L-glutamine, 2% B27-supplement and 100 ng/mL BDNF. Treatments were applied during the media exchange. After 24-hour incubation, the media was collected. Aβ40 was measured using SensoLyte® β-Amyloid (1-40) ELISA kits (AnaSpec). To achieve greater sensitivity for Aβ40 measurement, only 0.5 mL of media was added at time of treatment. Once collected, a protease inhibitor cocktail (Roche) was added to the samples to protect them while they were concentrated to 300 µL using an evaporator. All samples were aliquoted and frozen at -80°C if not used fresh and were only thawed once. After following the instructions provided with each kit, the plates were scanned using a GloMax Discover (Promega). A sigmoidal dose-response curve (constrained to bottom=0 because of subtraction of media-only blanks) was fit to the standards using Graphpad Prism 7.03 for Windows (Graphpad Software, La Jolla California USA, www.graphpad.com) and the curve was used to calculate the concentration of the samples. 2 technical replicates (2 wells) per biological replicate (media sample) were normalized to the vehicle (DMSO) control and averaged together before the three biological replicates were averaged for an n of 3. Samples slightly below background with a technical replicate slightly above background were treated as 0 rather than excluded.

Immunofluorescence imaging and analysis

All ICC imaging was performed on a Nikon Eclipse Ti inverted microscope equipped with a 100X Plan Apo VC objective (N.A. 1.40) and an Andor iXon+ 887 EMCCD camera. All imaging settings including power of the excitation light source, fluorescence filter sets (excitation, dichroic and emission filters, all from Semrock), exposure time and EM gain

were kept consistent for imaging different groups with the same immunofluorescence labeling. The optical filter sets (Chroma and Semrock) for Alexa 405/DAPI, 488, 568, and 647 fluorescence were, respectively: Ex 405/20X, DiC 425LP and Em 460/50; Ex 460/50, DiC 495LP and Em 535/25; Ex 565/25, DiC 585LP and Em 644/90; Ex 644/10 DiC 660LP and Em 710/50. Image analysis was performed in Fiji (Schindelin et al., 2012), a distribution of ImageJ (Schneider et al., 2012). First, four cell-free areas were selected as background regions and their mean fluorescence intensities were averaged to obtain an overall background fluorescence intensity value. Process ROIs were hand drawn in areas with a relatively low background. Synapse ROIs were hand-drawn from all synaptophysin1 puncta along the selected processes. Only synapse ROIs with an APP signal above background were quantified in most cases. For the purposes of defining nonsynaptic regions for quantification, all areas with a high Syp signal were subtracted from the process ROIs and the remainders were divided into sections of similar area. To avoid bias towards any field of view, an equal number of ROIs from each FOV (equal to the least number of ROIs per FOV) was randomly selected and pooled. The n for each condition is the total number of pooled ROIs. Background subtraction and random selection of ROIs was performed in Microsoft Excel. The values were imported into Prism 7.03 for plots and statistics. Statistical tests were chosen based on the experiment.

Object-based colocalization (**Supplementary Figure 1**) was performed using the Synapse Counter plug-in for ImageJ (Dzyubenko et al., 2016). No alterations were made to the images except to exclude transfected somas. Briefly, for 512x512 16bit images taken at 100x, the rolling ball radius was set to 8, the maximum filter radius to

1.0, Otsu threshold adjustment was used and minimum and maximum particle sizes were set to 5 and 400. For the purpose of this quantification, fields of view were used as the n rather than regions of interest as in other quantifications.

Filipin imaging (**Supplementary Figure 7**) was performed using AM1-43 to select FOV to minimize photobleaching in the Filipin channel. Due to the lack of synaptic markers, ROI selection was focused on the processes. Rather than hand drawing all processes as in quantifications that feature transfected cells only, the images were thresholded as a base, additional processes of lower intensity were added by hand, and the somas and debris were excluded. The processes were divided into ROIs of relatively uniform size. Areas with a lower density of astrocytes were intentionally selected but astrocytes could not be completely separated from the neurons.

Live cell imaging and analysis

Live cell imaging was performed with a Nikon Eclipse Ti inverted microscope, a 20X or 100X Plan Apo VC objective and an Andor iXon+ 887 EMCCD camera or a Hamamatsu Flash4 (**Figure 1D**). 12 mm coverslips were mounted in an RC-26G imaging chamber (Warner Instruments) bottom-sealed with a 24x40 mm size 0 cover glass (Fisher Scientific). The chamber was fixed to a PH-1 platform (Warner Instruments) placed on the microscope stage. Gravity perfusion-powered solution exchange was controlled by a VC-6 valve control system and a 6-channel manifold (Warner Instruments) with a constant rate of ~50 µL/sec which allowed a complete bath solution turnover in the recording chamber in under 30 s. Image acquisition and synchronized perfusion were controlled via

Micro-manager software. For every fluorophore, the acquisition settings including excitation power, fluorescence filter set (excitation, dichroic and emission filters), exposure time, camera gain and frame rate were all kept the same among different samples on all experiments. The optical filter sets (Chroma and Semrock) for Alexa 405/BFP2, pHluorin and pHTomato were, respectively: Ex 405/20X, DiC 425LP and Em 460/50; Ex 480/20X, DiC 495LP and Em 535/40; Ex 560/40M, DiC 585LP and Em 610/20nm BP. Samples were exposed to normal Tyrode's saline at pH 7.35, a 50mM NH_4Cl solution and normal Tyrode's solution adjusted to pH5.5 sequentially. Some of the older data sets in **Figure 4** and **Figure 2** were collected using NH_4Cl before 4K. Tyrode's saline contains (in mM): 150 NaCl, 4 KCl, 2 $MgCl_2$, 2 $CaCl_2$, 10 N-2 hydroxyethyl piperazine-n-2 ethanesulphonic acid (HEPES), 10 glucose, pH 7.35 or pH 5.5. The 50 mM NH_4Cl solutions was made by substituting for NaCl equimolarly, pH 7.35. All solutions contained 10 μM NBQX and 20 μM D-AP5 except in the experiment in **Figure 7 F-H**, which was meant to replicate the experiment in **Figure 7 A-E** during which MβCD was applied to the home media as a pretreatment in the absence of such activity altering drugs. StackReg (Thevenaz et al., 1998) was used to correct for state drift. MultiStackRegistration (Brad Busse) was used to align the pHluorin stacks using the pHTm stacks as reference, with individual frames adjusted as needed manually. For the purposes of quantification, the 3 most representative frames (5 for **Figure 4** and **Figure 2**) were chosen in each solution and averaged together in ImageJ. For example, as NH_4Cl is applied, fluorescence increases to a peak and then begins to decrease. Three consecutive frames with the highest fluorescence signal are used to represent of the maximum fluorescence. Because BFP2 signal is not pH-dependent, all BFP2 frames

were averaged together for quantification. Using averaged frames rather than taking the beginning, maximum and minimum from each trace reduces the error caused by actively moving puncta passing by a synapse. Average frames were used for all analyses except **Figure 3**, which is intended to detail acute responses to activity rather than to determine the surface and internal fractions of the fluorophores at a steady state as in the other figures. For live cell imaging analysis, synapses were defined based on the SypHTm signal; specifically, all static puncta. ROIs for synapses and neurites were manually selected in ImageJ. In addition, multiple cell-free areas were selected as background ROIs. Separate background ROIs were selected for BFP2 because astrocytes and untransfected neurons produced a high background in that channel; some ROIs chosen based on SypHTm were excluded due to the background in the blue channel in order to avoid individually defining the background for each ROI. Nonsynaptic ROIs were defined by manually drawing processes as seen on all 3 channels, subtracting out any regions suspected to be synapses, and dividing the remainder into similarly sized ROIs. Additionally, only ROIs with a detectable SypHTm signal in normal Tyrode's solution were included because puncta that are only visible in NH_4Cl are not necessarily synapses. For the purposes of defining nonsynaptic regions for quantification, all stationary SypHTm puncta were subtracted out. The somatodendritic regions were excluded, usually by choosing an imaging field without a transfected soma, due to high background and low prevalence of probable synapses compared to puncta visible only in NH_4Cl. The values of all ROIs, including background, for each image (average NH_4Cl, 4K, pH5.5 for SypHTm and pHluorin and stack average for BFP2) were exported to Microsoft Excel. The background was then subtracted, and then NH_4Cl – 4K was used to calculate the internal

protein and 4K – 5.5 was used to calculate the surface protein. For the purposes of quantification of APP in the synapses, only ROIs with a positive value for Total, Internal and Surface in the pHluorin and pHTm channels were included in the analysis. If the BFP2 signal was not higher than background, the ROI was also excluded. To avoid bias towards any field of view, an equal number of ROIs from each FOV was randomly selected and pooled. The n for each condition is the total number of pooled ROIs.

Kymographs were generated by manually tracing the processes using the Segmented Line tool in Fiji based on an averaged image of the BFP2 channel, using the “Reslice” command (Output Spacing = 1 pixel, Avoid interpolation). Paths of the moving puncta were traced by hand using the Segmented Line tool and saved to the ROI Manager. These selections were exported as XY coordinates with interpolation of 1 pixel. In order to be as accurate as possible, the actual time each image was taken was extracted and used to convert vertical pixel distances to time because the timing did not sync perfectly to the frame number across different fields of view. Because puncta sometimes split, appeared and disappeared, the n was determined separately at each time point for the purpose of calculating the mean and SEM. Puncta that disappeared were not counted as a zero but as a blank, while puncta that were still present but were not moving were included in the analysis. Synapses were determined using SypHTm puncta that did not move across the smaller number of frames collected of the channel. For each kymograph, the position of all synapses along the processes was listed on each spreadsheet page. Using Microsoft Excel’s array functions, the closest synapse to the puncta at any given time point was selected from the list. When a punctum moving between two synapses A

and B became closer to B than A, it was then considered to be moving in the positive direction towards the nearest synapse. The position of the puncta with respect to the soma was not considered for the purpose of this calculation because the experimental question was whether lateral movement toward or away from the synapse. There was no marker used in any live cell imaging that can separate axons from dendrites, so no claim is made about the identity of the processes quantified. However, due to the distance from the soma needed to get lower backgrounds, the narrow and consistent width of the selected processes, and the expression pattern of SypHTm, they are most likely axons.

The analysis of **Figure 7A-D** was performed differently because the size was the most important feature to be quantified, and hand drawn ROIs were therefore unsuitable. The images were also collected differently (detailed below). First, Convoluted Background Subtraction from the BioVoxxel Toolbox (http://imagej.net/BioVoxxel_Toolbox) was used, followed by Non-local Means Denoising (Buades et al., 2011; Darbon et al., 2008), bandpass filter, auto-local threshold using the Bernsen method, Adjustable Watershed (Michael Schmid) with a tolerance of 0.1. Using a macro, the same procedure was applied to all images and then debris were manually removed, non-static ROIs were excluded, and compounded ROIs that escaped the watershed were manually separated. The measure tool was then used to collect the data. All of the intensity values were taken from the original, unaltered images. During the collection of this data, multiple fields of view were observed from the same coverslip between solution changes using the Position List feature on Micro-Manager to return to the locations. 10 frames were collected from each channel at each field of view in each solution, aligned and averaged. To correct for

cumulative photobleaching, values for NH4Cl and pH 5.5 were multiplied by arbitrary factors so that the quantification can still be performed. Furthermore, due to morphology changes over time during this extended imaging, the ROIs were manually moved as the processes moved based on the pHTm channel, which the other channels were aligned to. Additionally, due to the high signal to noise ratio each ROI had its own background ROI defined by shifting all ROIs in the manager about 10 pixels over in the x and y directions and manually moving the background ROIs from there to the most suitable area with a similar background (for example, a transfected cell-free area on the same auto fluorescing flat glial cell as the synapse). After the background subtraction and arbitrary photobleach correction was equally applied to all conditions, ROIs were excluded as before for having below background signal in any of the channels. Because of this, it is difficult to compare the fluorescence results from this figure to other experiments in the paper directly. For this experiment, it was very important to select FOV without consideration to factors such as the size of the synapses, process health and morphology. Because fields of view were not chosen based on the quantity of synapses but rather on the presence of transfected punctated structures at all, ROIs were not randomly selected from each field of view and instead all were included and pooled.

Statistical tests

Statistical tests were performed using Graphpad Prism 7.03. Each test is listed in the figure legends, but in general two-tailed t-tests were used to compare two conditions, one-way ANOVA and Dunnett's multiple comparisons test was used to compare the control condition to multiple other conditions, and two-way ANOVA and Sidak’s multiple

comparisons test was used to compare results within one variable in experiments with two variables.

Supplementary Information

The supplementary materials including supplementary figures and legends, supplementary tables and supplementary movies.